



Role of compression metallization in UO₂ fission-product energy cascade track: Multiscale electron-phonon analyses

Woong Kee Kim ^{a,1}, Corey Melnick ^{b,1}, Ji Hoon Shim ^{a,c}, Massoud Kaviani ^{a,b,*}

^a Division of Advanced Nuclear Engineering, Pohang University of Science and Technology, Pohang 37673, South Korea

^b Department of Mechanical Engineering, University of Michigan, Ann Arbor, MI 48109-2125, USA

^c Department of Chemistry, Pohang University of Science and Technology, Pohang 37673, South Korea



ARTICLE INFO

Article history:

Received 8 December 2017

Received in revised form

30 April 2018

Accepted 5 September 2018

Available online 7 September 2018

Keywords:

Compression metallization

ab-initio

Classical molecular dynamics

Two temperature model

Swift heavy ion

Fission product

Electronic stopping

Irradiation

ABSTRACT

While the electronic stoppage of charged fission fragments is relatively well understood, the subsequent energy cascade is not. Recent efforts to investigate this cascade and predict the resulting damage have used a two-temperature model (TTM) of the electronic and phononic systems coupled with a classical molecular dynamics (MD) simulation of the crystal lattice. In order to accurately predict the track radius produced by a fission fragment in UO₂, this model (TTM + MD) requires that UO₂, an insulator, have metallic properties, e.g., a substantial electron thermal conductivity and heat capacity. However, it has been predicted that UO₂ becomes metallic under large pressures, and we perform *ab initio* (DFT-HSE) simulations to support this prediction. We show that the average U-U bond length decreases within and near the ion track during TTM + MD simulations, supporting the use of volume contraction to model the pressurized UO₂ cell. Additionally, we evaluate the electron, phonon, and electron-phonon coupling properties of UO₂ for variations in the pressure. In particular, we calculate the electronic heat capacity and thermal conductivity, and the electron-phonon energy coupling for use in subsequent TTM + MD simulations. The *ab initio* parameterized TTM + MD simulations provide a set of the track radii predictions which bracket and include the experimentally observed radii. The accuracy of the *ab initio* parameterized TTM + MD simulations depends on the pressure and degree of electron-phonon non-equilibrium assumed during the *ab initio* calculations. We suggest improvements to the current TTM + MD methodology in light of these results. Still, we show that the pressure-induced transition of UO₂ from insulator to metal and subsequent energy transfer from the electronic to phononic systems can accurately explain radiation damage during swift, heavy ion stoppage in UO₂. We make some additional observations regarding the accumulation and recombination of damage along the ion track and make comparison to the common SRIM model of ion stoppage and damage accumulation.

© 2018 Elsevier B.V. All rights reserved.

1. Introduction

During nuclear fission, extremely energetic fission fragments (fast, heavy ions), photons (γ rays), and neutrons are released [1]. The energetic fission fragments contain the majority of the initial fission energy, and these charged particles quickly slow down through their interaction with and ionization of atoms in the host material [2,3]. The resulting, high energy electrons (δ rays), in turn

collide with and excite more electrons [4]. Further, tertiary ionization events can occur, such that the fission fragment is said to create an electron shower or cascade in its wake. These electronic interactions typically occur on the order of a femtosecond, and the fission fragments quickly lose energy. Eventually, they reach an energy where they are more likely to collide with the atoms of the host material rather than ionize them [5]. Such atomic collisions create an atomic, rather than electronic, cascade: The impacted nuclei are ejected from their sites in the lattice and subsequently collide with other nuclei, ejecting them from their lattice site [6,7]. At the end of the electronic and atomic cascades, the energetic carriers (electron or nuclei) do not have sufficient energy to dislodge a new energy carrier. Instead, they excite vibrations, or phonons, in the crystal lattice. The phonons then interact with the

* Corresponding author. Department of Mechanical Engineering, University of Michigan, Ann Arbor, MI 48109-2125, USA.

E-mail address: kaviani@umich.edu (M. Kaviani).

¹ Equally contributed to the work.

crystal anharmonicity and down-convert into the lower-energy acoustic branches [8]. Eventually, the electron and phonon systems thermalize, with an average carrier energy given by the thermal energy, $k_B T$, where k_B is the Boltzmann constant and T is the temperature. The broad outline of this relaxation pathway is shown in Fig. 1, as adapted from Ref. [9].

This process disrupts of the atomic lattice of the material. Indeed, the atomic collisions create defects, and the electron plasma formed by the electron cascades deposits a massive amount of energy into the phonon system as it cools, and this leads to local melting and atomic ejections along the path of the fission fragment, as shown in Fig. 2. While the melted region partially recovers, the accumulation of defects and melted region degrades the integrity of the nuclear fuel over time [10]. Thus, predicting the extent of the damage to the fuel, understanding the mechanisms through which this damage occurs, and creating strategies for damage mitigation or recovery are of interest in material science and nuclear engineering [11–17].

Radiation damage has been studied using classical molecular dynamics (MD) and the stopping and range of ions in matter (SRIM) codes [18]. Both methods offer insight, but they are also limited. In MD, for example, the electronic stopping cannot be simulated, but the collision cascade which follows is accurately modelled [19]. While the SRIM codes simulate the interaction of the fission fragment with both nuclei and electrons, they do not provide an atomistic description of the material. Thus, they cannot capture of the influence of the crystalline direction, the creation of defect clusters, or their recombination [20,21]. Recently, a two-temperature model (TTM) of the coupled electron and phonon populations was connected to the classical MD treatment in order to overcome such limitations.

In the TTM + MD model, the electronic energy deposited along the fission-fragment pathway is taken as an initial condition of the

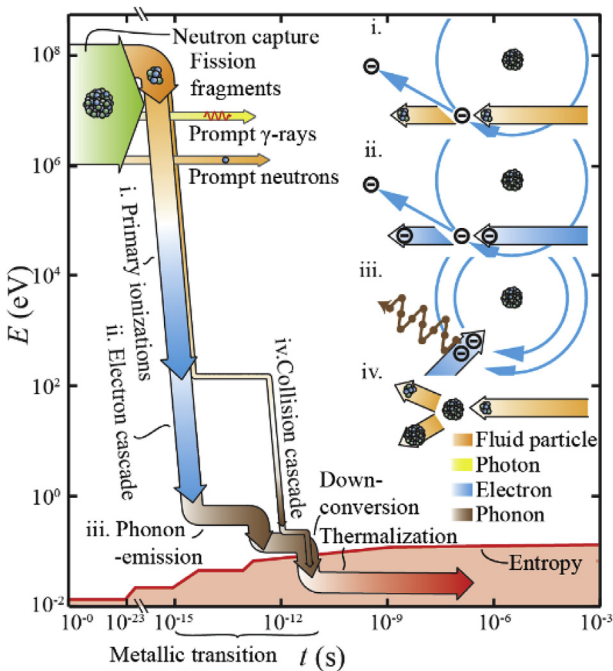


Fig. 1. Evolution in the fission energy (E) as it ultimately converts to heat over time (t), the fission fragments and their fate, and the increase in the entropy of the system as thermalization is reached, adapted from Ref. [9]. The majority of fission energy is deposited in the fission fragments which induce an electronic and then nuclear cascade as they penetrate into a material. Eventually, this energy must become heat, i.e., a large, entropic collection of atomic vibrations or phonons.

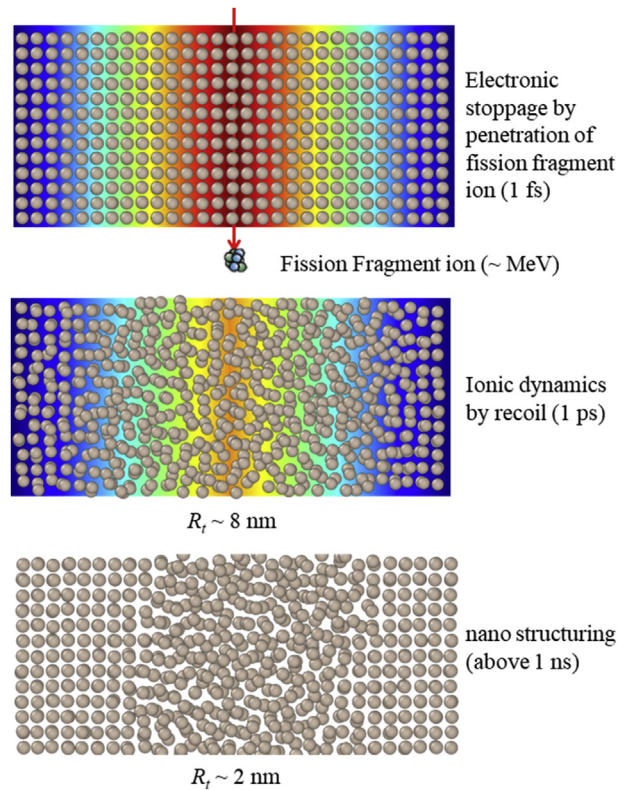


Fig. 2. The energy cascade following the electronic stoppage of a fission fragment energy in bulk UO_2 . Through stoppage by bound electrons, the ion energy is first transferred to the electron system, which causes lattice distortion, ion ejection, and melting. This process may induce metallization along the ion track. The lattice is partially recovered around the ion track radius R_t .

TTM model, the atomic positions in pristine UO_2 are used as an initial condition for the MD simulation, and the simulation proceeds by alternately marching time forward in the coupled TTM and MD simulations. A Langevin thermostat couples the background solvent (the electronic subsystem) to the Langevin dynamics of the atoms (the phononic subsystem). Thus, it allows for an atomistic perspective of the radiation damage without neglecting the dominant mechanism for fission fragment stoppage: electronic stoppage. For an accurate prediction of the track radii produced by swift heavy ions in UO_2 , a dielectric, the TTM + MD model requires that the ion target has an electronic heat capacity, thermal conductivity, and the electron-phonon energy coupling comparable to those of a metal [2,10,13,22]. Below we note two possible mechanisms for this metallic behavior.

First, the electronic stoppage and the resulting electron cascade create a large concentration of free electrons very near the ion path. Indeed, simulations of the electron cascade created by a fission fragment penetrating polyethylene (a dielectric) show that the resulting radiation dose, E/V , is sufficiently large to induce a metallic electron concentration, $n_{e,C}$, of 10^{28} or more electrons per m^3 within a radius of nearly a nm [4], as shown in Fig. 3. (We arrive at this estimate by dividing the radiation dose by the average kinetic energy of the ejected electron in the aforementioned simulations, i.e., 12 eV) Another simulation of the electron cascade created by a δ -ray in diamond (another dielectric) [3], predicts that a single 1 keV electron can produce narrow regions with substantial $n_{e,C}$, 10^{26} – 10^{24} $1/\text{m}^3$. As a fission fragment creates a high concentration of δ -rays [4], the excited electron population along its path will have a heat capacity, thermal conductivity, and electron-phonon coupling like that of the electron population in a metal.

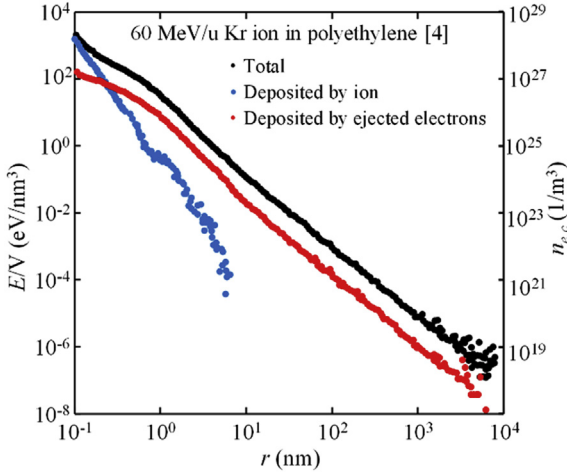


Fig. 3. The ion energy deposition distribution of a Kr ion with an initial energy of 60 MeV/u penetrating a polyethylene target [4] and an estimate of the resulting electron density. High electron concentrations are produced near the track core, which may lead to metal-like material properties.

However, this excited electron population is short lived and confined to the track core. In Refs. [3] and [4], for example, the excited concentration resides only within a few nm of the track core. In Ref. [3], this concentration spreads quickly and the peak concentration falls by an order of magnitude within 10 fs.

An alternate mechanism which leads to a longer lived metallic state is as follows: the fission fragment creates a high-pressure wake (due to the electron-phonon coupling) which induces a metallic transition in UO_2 . Supporting this hypothesis are recent density functional theory (DFT) calculations using dynamical mean field theory (DMFT). These simulations predict that pressures in excess of 45 GPa induce a transition in the electronic structure of UO_2 , turning it from an insulator into a metal [23]. As TTM + MD simulations show that such pressures are induced during the electronic stoppage of fast, heavy ions in UO_2 , this is a promising explanation for the metallic properties required to produce an accurate TTM + MD model of ion stoppage in UO_2 .

However, the predicted, DMFT transition occurs due to the decrease in the cell volume. It does not arise directly from the increase in the pressure. The fission fragment, in contrast, induces a high pressure by quickly increasing the system temperature before the volume can respond. Thus, the cell volume does not decrease within the wake. While we might expect it to increase in the wake of the fission fragment, TTM + MD simulations show that damage accumulates within the ion track before this occurs. This damage, as we will show, largely accumulates via the ejection of hot oxygen ions from within the ion track. Interestingly, this leads to a net decrease in the distance between Uranium atoms within and near the ion track. Unfortunately, it remains impossible to accurately simulate the resulting, amorphized ion track. We hypothesize that compressed UO_2 roughly approximates the effects of the pressurized and damaged UO_2 in the wake of a fission fragment.

In this work, we investigate this hypothesis and the radiation damage caused by a fission fragment penetrating UO_2 . In particular, we perform *ab initio* simulations (DFT-HSE) of UO_2 , reproducing the metallic transition predicted within DFT-DMFT and calculating the pressure dependent electron, phonon, and electron-phonon coupling properties. We then use these properties in TTM + MD simulations of the electronic stoppage of fission fragments in UO_2 . These two treatments are used to explore the origin of the metallic behavior in UO_2 and the mechanisms driving radiation damage. We note, however, that this is only a first effort at the *ab initio*

parametrization of TTM + MD models and the *ab initio* investigation of radiation damage in UO_2 . Further research is necessary to investigate the damage caused by fission fragments and the relationship between the damage and the corresponding electronic structure and transport properties. Furthermore, we conduct discretized set of the nm-scale TTM + MD simulations at different energies in order to explore defect production within the μm -scale ion tracks created by typical fission fragments. First, however, we discuss our *ab initio* calculations of UO_2 and present the predicted material properties used in our TTM + MD simulations.

2. UO_2 *ab initio* calculations

2.1. Electronic properties of UO_2

Based on its chemical composition, one might expect that UO_2 is a metal with its two unbound electrons partially filling the *f*-bands. However, the strong correlation between the *f*-band electrons in UO_2 opens a substantial bandgap between the two occupied *f*-bands and the remaining, unoccupied *f*-bands. That is, UO_2 is a Mott insulator [24–27]. This strong-correlation precludes the accurate simulation of UO_2 using traditional density functional theory (DFT) methods which use the local density or general gradient approximations (LDA, GGA) of the exchange-correlation functional [26]. However, extensions of DFT have been used to successfully simulate UO_2 . These include the DFT + U method [28], the DFT (LDA) + DMFT method [23], and the DFT with hybrid functional methods [29]. Here, we use a hybrid functional approach, wherein the meta-GGA functional and Hartree-Fock (HF) functional are combined in order to capture the correlation effects. In particular, we use the Heyd-Scuseria-Ernzerhof (HSE) exchange correlation [30], which mixes the screened, short-range HF exchange and the short-range Perdew-Burke-Ernzerhof (PBE, a meta-GGA functional) [30] exchange functional and combines this mixture with the long-range PBE exchange and complete PBE correlation functionals. We use the standard HSE06 parameterization [29] which has been shown to work well for the actinides, including UO_2 .

Briefly, let us overview the remaining simulation methodology. For the electronic properties, we use the *ab initio* simulation code Quantum-Espresso [36,37]. The wavefunctions are modelled using a plane-wave basis set with a kinetic energy cut-off of 120 Ry. Scalar relativistic, norm-conserving Martins-Toullier [38] pseudopotentials are constructed for uranium, configuration [Rn] $5f^3 6d^1 7s^2$, and oxygen, configuration [He] $2s^2 2p^4$. The simulations are carried out on a $6 \times 6 \times 6$ (6^3) κ_e -mesh with the HF exchange considered on a fully commensurate (6^3) q_e -mesh at each κ_e -point. When evaluating material properties like the density of states, heat capacity, thermal conductivity, or electron-phonon coupling, the resulting mesh of electron eigenvalues is interpolated onto a 30^3 κ_e -mesh. The ground state lattice constant, $a = 5.65 \text{ \AA}$, is found by comparing the crystal energy for variations in a , as shown in Fig. 4. We do not include the

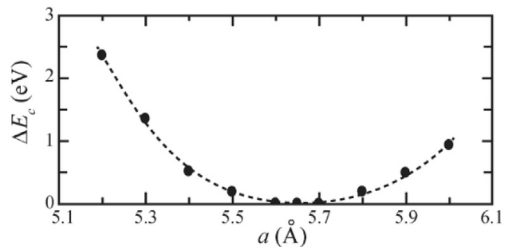


Fig. 4. Crystal energy for variations in the lattice constant. The energy is offset by the minimum found at $a = 5.65 \text{ \AA}$. The calculated bulk modulus is 181.1 GPa.

spin-orbit coupling, as it would reduce our ability to simulate reasonably dense κ_e and q_e -meshes, particularly in our electron-phonon coupling simulations. Still, the physical and electronic properties predicted within our simulations match reasonably well with those recorded in experiments and in other, previously published *ab initio* calculations, as shown in Table 1.

Indeed, while the electronic density of states, D_e , deviates from the experimentally resolved density of states [39], it still maintains some of the crucial features, as shown in Fig. 5(b). In particular, the bandgap, ΔE_{eg} , is well captured. However, the f -bands are more confined within the DFT-HSE simulations than they are in experiments. Indeed, the low-energy conduction bands are nearly flat, as shown in Fig. 5(a). These results match reasonably well with previously published DFT-HSE results [26,27], despite the lack of the spin-orbit coupling. Thus, we proceed to the investigation of the metallic transition.

Before continuing, let us discuss the role of the thermal smearing and electron occupation in determining the electronic band structure. Within DFT-HSE simulations, the electron occupation can either be fixed, with the valence (conduction) bands set to be fully occupied (unoccupied), or it can be calculated using, e.g., the Fermi-Dirac distribution. The fixed approximation reproduces the correct occupations of a 0 K insulator, but it is a poor approximation in metals or semi-metals, where one would expect the conduction states below the Fermi level to be occupied and the valence states above it to be unoccupied, even at 0 K. Still, it can be used to accurately calculate the ground-state electronic structure of a semi-conductor or insulator. Fig. 6(a) and (b) show the electronic structure of UO_2 for variations in the lattice parameter when we use the fixed approximation.

As shown in these figures, DFT-HSE simulations under the fixed occupation approximation predicts that UO_2 undergoes a smooth transition from an insulator to a semi-metal as the pressure increases. This transition occurs as the low energy valence and conduction states spread out towards the Fermi level, with the valence bands approaching the Fermi level near the zone-center (Γ) and the conduction bands approaching the Fermi level near L. Indeed, a direct energy gap remains between these bands, even as the band gap vanishes. This matches the DFT-DMFT results relatively well [23]. The principal differences are as follows: DFT-HSE predicts that a 10% reduction in volume is sufficient to induce this transition, whereas DFT-DMFT predicts that a 15% reduction is necessary; and the DFT-HSE simulations predict that a smaller direct energy gap remains between the conduction and valence bands after the transition occurs. This semi-metallic behavior persists if we continue to use fixed occupations, with a direct energy gap remaining between the valence and conduction bands. However, it becomes inappropriate to use fixed occupations when simulating pressurized UO_2 after it undergoes this transition, as the conduction states with less energetic than the Fermi level should become occupied and the valence states more energetic than the Fermi level should become unoccupied. Thus, we must treat the DFT-HSE semi-metallic UO_2 results with some skepticism after the valence and conduction states begin to overlap in energy.

Table 1

The lattice constant (a), bulk modulus (B), cohesive energy (ΔE_f), and band gap (ΔE_{eg}) of UO_2 as determined in previous computational studies, in experiments, and in the present work.

Source	a (Å)	B (GPa)	ΔE_f (Ry)	ΔE_{eg} (eV)
DFT + U [31]	5.540	191.6	−1.63	2.3
DFT-HSE [32]	5.463	218.0	—	2.4
DFT-DMFT [23]	5.571	183.8	—	2.1
Experiment	5.473 [33]	207.2 [33]	−1.64 [34]<	2.1 [35]
Present work	5.645	181.1	−1.71	2.26

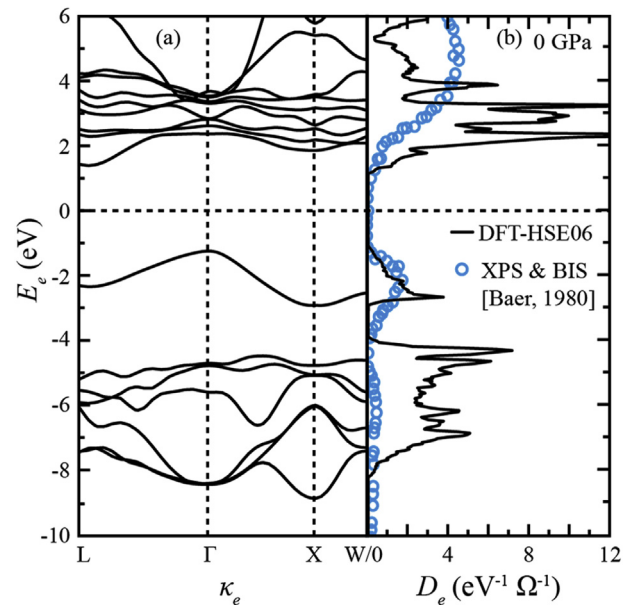


Fig. 5. Electron (a) band structure and (b) density of states as predicted within DFT-HSE. The experimental, f -band density of states is shown for comparison [4]. DFT-HSE accurately predicts the bandgap of UO_2 , but over predicts the localization of the conduction f bands.

If we allow for some thermal smearing using, e.g., the Fermi-Dirac distribution with some electron temperature, our predictions are substantially complicated by the appearance of the metastable metallic state shown in Fig. 6(c). We note that this metallic state largely resembles that predicted within DFT-GGA or DFT-LDA, i.e., traditional DFT simulations which do not include the HF exchange, and that it is insensitive to the degree of thermal smearing or pressure. Furthermore, we note that DFT-HSE simulations of the insulative, unpressurized UO_2 can converge to this metallic state if a small thermal smearing is used and one is not sufficiently careful with the simulation procedure. Indeed, our simulations of insulative UO_2 typically converge to this metastable, metallic state regardless of the convergence criterion, particularly at higher pressures where the energy difference between the solutions is smaller. Consider, for example, that the semi-metallic, high pressure solution ($a = 5.18 \text{ \AA}$, fixed occupations) was separated from its metallic counterpart (Fermi-Dirac occupations) by a total energy of only 0.13 eV, substantially less than the 0.92 eV separating the unpressurized ($a = 5.65 \text{ \AA}$) insulative UO_2 solution (fixed occupations) from its metallic counterpart (Fermi-Dirac occupations).

We hypothesize that the metastable state arises through the following mechanism: The thermal excitation of electrons into the conduction bands drastically changes the exchange energy between these electrons and those in the partially unoccupied valence states, such that the conduction band is pulled towards the valence bands; this leads to further population of the conduction band and further reduction in the exchange energy cost of the metallic state; and this eventually induces the transition into a fully metallic state. As little is known about highly pressurized UO_2 and the resulting metallic or semi-metallic transition, it is difficult to say whether this metastable state can exist in reality, if it becomes stable at sufficiently high pressures, or if it is a purely numerical phenomenon. While the DFT-DMFT simulations suggest that the semi-metallic state persists after the semi-metallic transition occurs [23], experimental data on the electronic properties of highly compressed UO_2 is required to investigate the potential existence of

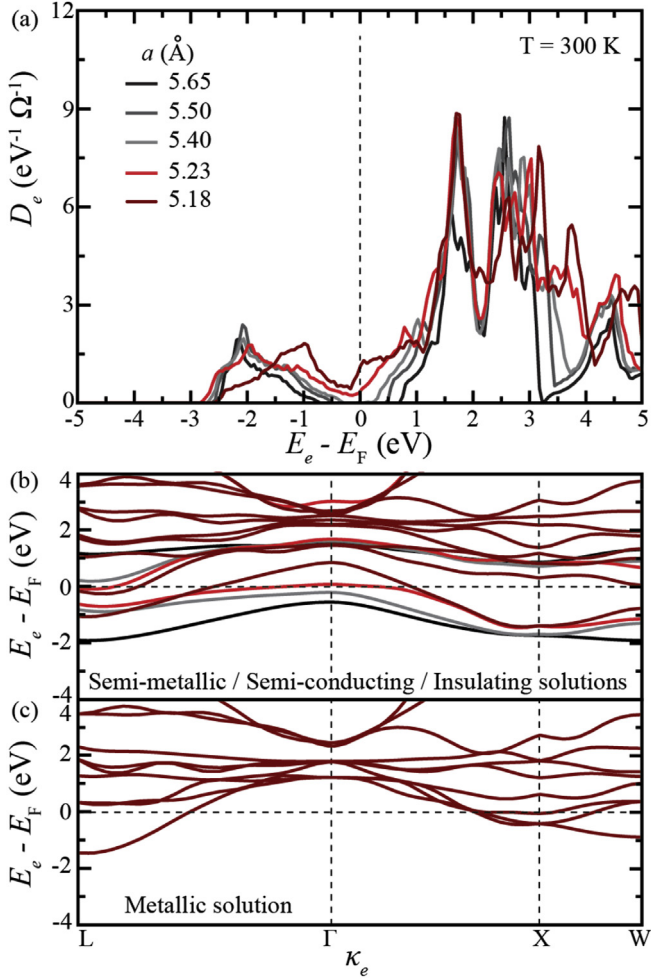


Fig. 6. (a) Electron density of states and (b), (c) bandstructure of UO_2 for variations in the lattice constant, where only the first valence and conduction bands are shown for the semi-conducting and insulating UO_2 . UO_2 becomes semi-metallic for $a < 5.23 \text{ \AA}$, with a sizeable direct energy gap between conduction and valence states. Under high pressures ($a = 5.18$) and with thermal smearing, DFT-HSE predicts a complete collapse of this Mott-insulator like gap and the transition from semi-metal to metal. Our simulations suggest that this metallic solution is a metastable state.

this metallic state following the semi-metallic transition. Thus, we must treat our metallic results with skepticism. Thus, we will primarily discuss the properties of the semi-metallic, semi-conducting, and insulating UO_2 using the fixed occupation approach. Moreover, we will limit ourselves to $5.65 \geq a \geq 5.23$, i.e., from un-compressed UO_2 to the pressure at which semi-metallic transition occurs, as we cannot reliably simulate the higher pressure semi-metallic states. We will also present the properties of the metallic state ($a = 5.18$), which could represent the limiting behavior of semi-metallic UO_2 , even if it may be non-physical. (Unless otherwise specified, the $a = 5.18$ results presented below are for the metallic solution.)

Now, let us discuss the electronic heat capacity before moving onto those parameters which require knowledge of the electron-phonon coupling. The electronic heat capacity (C_e) is given by the following sum [39].

$$C_e = \sum_{\kappa_e, i} (E_{e, \kappa_e, i} - E_F) \frac{\partial f_e^0}{\partial T}, \quad (1)$$

where $E_{e, \kappa_e, i}$ is the energy of an electron in wavevector κ_e and band

i, f_e^0 is the occupation of an electron with energy $E_{e, \kappa_e, i}$ in an electron population with temperature T and Fermi energy E_F , as given by the Fermi-Dirac distribution. Here we use the code BoltzTrap [40] to carry out this integral for the set of $E_{e, \kappa_e, i}$ collected from our DFT-HSE calculations. The results are fit to the curve

$$C_e = C_0 + \left(C_1 T_e + C_2 T_e^2 + C_3 T_e^3 + C_4 T_e^4 - C_0 \right) \exp \left[- \left(\frac{T_e}{T_0} \right)^2 \right]. \quad (2)$$

As shown in Fig. 7, the heat capacity is relatively insensitive to the volume once the semi-metallic transition occurs. Before this transition, the electronic population in UO_2 has a negligible heat capacity until the thermal energy, $k_B T$, approaches the bandgap, at which point the valence electrons begin to populate the conduction bands and the heat capacity becomes substantial.

In Fig. 7, we also compare the predicted heat capacity with those used in previous TTM-MD studies of radiation damage in UO_2 [2,10]. As shown, the DFT-HSE heat capacities are comparable to but smaller than the previously used values. We will show that heat capacities of this order of magnitude are required to achieve accurate radiation damage predictions using the TTM + MD, and that variance within this order greatly influences these predictions. Moreover, the previous TTM + MD heat capacities were chosen in order to predict accurate track radii, i.e., they have not been based on or extracted from experimental results.

Now, let us discuss the electronic thermal conductivity, k_e , as given by the following summation [39].

$$k_{e,xy} = \frac{2}{T} \sum_{\kappa_e, i} (E_{e, \kappa_e, i} - E_F)^2 u_{\kappa_e, i, x} u_{\kappa_e, i, y} \tau_e \frac{\partial f_e^0}{\partial E}, \quad (3)$$

where τ_e and $u_{\kappa_e, i, x}$ are the lifetime and group velocity along x for an electron in band i and wavevector κ_e . Assuming the lifetime is constant, we can extract it from this integral, and the remaining terms can be evaluated using the $E_{e, \kappa_e, i}$ calculated within DFT-HSE. Here, we take this constant-lifetime assumption and evaluate the

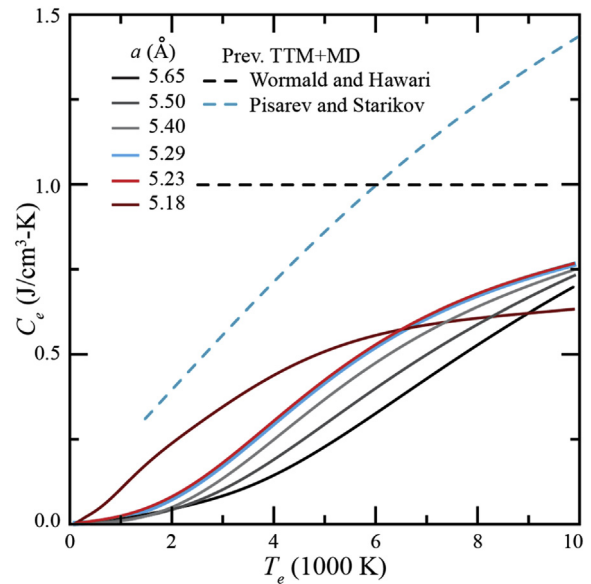


Fig. 7. Heat capacity for variations in the electronic temperature and lattice parameter. Heat capacities used in previous TTM + MD simulations are also shown [2,10]. The predicted heat capacities for semi-metallic UO_2 are comparable to but smaller to those used in previous TTM-MD studies of radiation damage in UO_2 .

sum using BoltzTrap [40]. However, the evaluation of the lifetime itself remains. Here we only consider the scattering between electrons and phonons and neglect, e.g., the scattering between electrons and defects. Thus, let us discuss the electron-phonon coupling before presenting the thermal conductivity results.

2.2. Electron-phonon coupling in UO_2

The electron-phonon coupling (EPC) is difficult to evaluate in UO_2 due to the failure of traditional GGA or LDA exchange-correlation functionals. Consider the EPC matrix element $M_{e-p}^{ij,\alpha}(\kappa_e, \kappa_p)$ which describes the scattering of an electron in an initial state $|i, \kappa_e\rangle$ into a final state $|j, \kappa_e + \kappa_p\rangle$ by a phonon with momentum κ_p and polarization α . Within perturbation theory, this matrix element is

$$M_{e-p}^{ij,\alpha}(\kappa_e, \kappa_p) = \left(\frac{\hbar}{2m\omega_{\alpha,\kappa_p}} \right)^{1/2} \kappa_e + \kappa_p, j | \frac{\partial H_e}{\partial \mathbf{e}_{\kappa_p}^\alpha} | \kappa_e, i, \quad (4)$$

where H_e is the electron Hamiltonian (e.g., the Kohn-Sham potential in DFT [41]), m is the average atomic mass, and $\omega_{\alpha,\kappa}$ and $\mathbf{e}_{\kappa_p}^\alpha$ are the phonon frequency and eigenvector. To calculate these elements we need dynamical matrices describing the phonon eigenproblem and the operator $\partial H_e / \partial \mathbf{e}$. Both tasks are traditionally done using density-functional perturbation theory (DFPT). However, DFPT calculations require enormous computational expense compared to DFT calculations. This prohibits the inclusion of the HF exchange-correlation in a DFPT calculation. Here we turn to an alternate approach which should provide order-of-magnitude estimates of the EPC.

In this approximation, we limit our evaluation to the EPC between electrons in the same state with the zone-center phonons, i.e., $M_{e-p}^{ij,\alpha}(\kappa_e, \kappa_p = \Gamma)$. Under this restriction, we can rewrite the approximate EPC as

$$M_{e-p}^{ii,\alpha}(\kappa_e, \Gamma) = \left(\frac{\hbar}{2m\omega_{\alpha,\Gamma}} \right)^{1/2} \kappa_e, i | \delta H_e(\Delta e_\Gamma^\alpha) - H_e | \kappa_e, i, \quad (5)$$

where $\delta H_e(\Delta e_\Gamma^\alpha)$ is the electric Hamiltonian when the atoms are displaced by the phonon eigenvector \mathbf{e}_Γ^α normalized by a distance of Δe_Γ^α . Noting that $\kappa_e, i | \delta H_e(\Delta e_\Gamma^\alpha) | \kappa_e, i = \delta E_{e,\kappa_e,i}$ and $\kappa_e, i | H_e | \kappa_e, i = E_{e,\kappa_e,i}$, the restricted EPC matrix elements can be evaluated through self-consistent DFT-HSE simulations of perturbed and unperturbed UO_2 , respectively. However, we still require the phonon eigenvectors and frequencies in order to perturb the atoms, construct $\delta H_e(\Delta e_\Gamma^\alpha)$, and then evaluate $\delta E_{e,\kappa_e,i}$.

To do this, we generate a $4^3 \times 4^3$ -mesh of dynamical matrices using DFT-GGA (PBE) simulations. The electrons are treated on a 24^3 κ_e -mesh with a plane wave basis extending up to 150 Ry using scalar-relativistic, plane-augmented wave (PAW) ultrasoft pseudopotentials. We change pseudopotentials here in order to calculate a more accurate phonon dispersion than we are able to with the previous, norm-conserving pseudopotentials. The structure is relaxed to its ground state at atmospheric pressure, requiring electronic self-consistency within 10^{-9} Ry and atomic forces within 10^{-8} Ry/Bohr. We find a reduced lattice constant of 5.56 Å, primarily due to the underestimation of the electron correlation, as discussed in the literature [26].

Using this methodology, we calculate the phonon dispersion using the Fourier interpolation scheme implemented in Quantum Espresso [37], and the results are shown in Fig. 8. As shown in Fig. 8(a), our phonon dispersion agrees acceptably with experiment. While the highest optical branch is poorly resolved, as seen in

other DFT studies [23], the other long-wavelength phonon modes are well resolved, with a slight red-shift. While the acoustic-optical phonon bandgap grows as the pressure increases, the density of states, D_p , retains a similar shape as the pressure increases, as shown in Fig. 8(b). Still, there is a notable blue-shift in the phonon frequencies, ω_p , as pressure is applied.

As these are the modes with which we will estimate the EPC, we can reasonably proceed with our calculations of the electron-lifetime.

From the Fermi golden rule, the electron-phonon scattering rate is

$$\dot{\gamma}_{e-p}(\kappa_e) = \frac{2\pi}{\hbar} \sum_{\kappa_p,\alpha} \left| M_{e-p}^{ij,\alpha}(\kappa_e, \kappa_p) \right|^2 \delta(E_{e,\kappa_e,i} - E_{e,\kappa_e+\kappa_p,j} + \hbar\omega_{\kappa_p,\alpha}) \times \left(1 - f_{e,\kappa_e+\kappa_p,j} \right) \left(\frac{1}{2} + \frac{1}{2} f_{p,\alpha,\kappa_p} \right), \quad (6)$$

where f_{p,α,κ_p} is the phonon occupancy given by the Bose-Einstein distribution [2] and the δ function conserves energy during phonon absorption (+) or emission (-) events. Note that energy cannot be conserved for scattering between a state and itself, unless the phonon frequency vanishes. Moreover, the zone-center acoustic modes where this is true should not affect the electron Hamiltonian, as all atoms are displaced by the same vector. Thus, our EPC coupling calculations are heavily approximated: Not only are we restricted to the zone-center phonon modes, but we are also gathering EPC matrix elements that technically cannot contribute to the electron-phonon scattering events. However, energy can be conserved when electrons scatter with long-wavelength phonon modes near the zone-center, and it can be reasonably approximated that the long-wavelength EPC matrix elements equals their

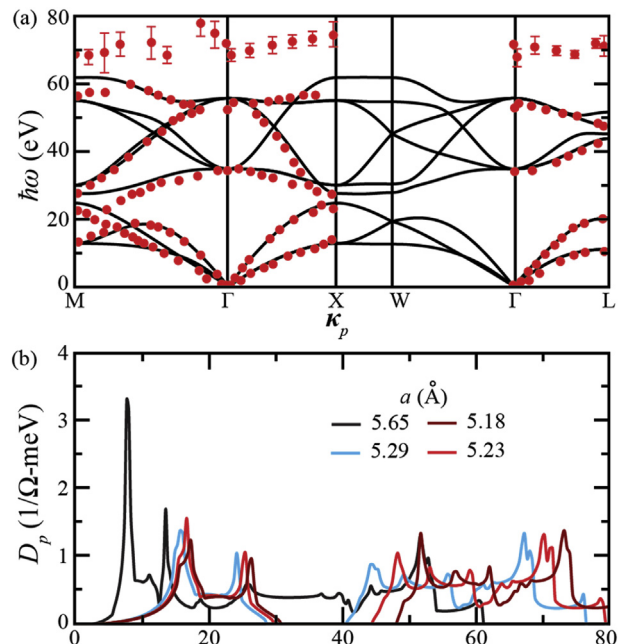


Fig. 8. (a) Phonon dispersion as compared to experimental data throughout the BZ [42] and for the Raman/IR modes at Γ [43]. The highest optical branch is poorly resolved within DFT simulations, but much of the phonon dispersion is accurately predicted. (b) Phonon density of states, D_p , for variation in the lattice constant. High pressure blue-shifts the phonon frequencies, ω_p , notably. (For interpretation of the references to colour in this figure legend, the reader is referred to the Web version of this article.)

infinite-wavelength (Γ -point) EPC matrix element counterparts. We extend this approximation and take a deformation potential approach [44]. That is, we assume that the EPC for a given polarization is approximately independent of the wavevector or band, writing

$$\dot{\gamma}_{e-p}(E_e) \approx \sum_{\alpha,\nu} M_{e-p}^{\alpha} D_{e,\nu}(E_e \pm \hbar\omega_{\alpha}) \left[1 - f_e^{\circ}(E_e \pm \hbar\omega_{\alpha}) \right] \left(\frac{1}{2} + \frac{1}{2} + f_{p,\alpha}^{\circ} \right), \quad (7)$$

where M_{e-p}^{α} is the average EPC in the actively scattering states. That is,

$$M_{e-p}^{\alpha} = \sum_{i,\kappa_e} D_e f_e^{\circ} \left(1 - f_e^{\circ} \right) \left| M_{e-p}^{ii,\alpha}(\kappa_e, \Gamma) \right| \Bigg/ \sum_{i,\kappa_e} D_e f_e^{\circ} \left(1 - f_e^{\circ} \right). \quad (8)$$

We then define the average scattering rate (weighted by the electron population) as

$$\dot{\gamma}_{e-p} = \frac{\int_{-\infty}^{\infty} f_e^{\circ} D_e \dot{\gamma}_{e-p}(E_e) dE_e}{\int_{-\infty}^{\infty} f_e^{\circ} D_e dE_e}. \quad (9)$$

Finally, we neglect other scattering mechanisms, such that $\tau_e = 1/\dot{\gamma}_{e-p}$. Fig. 9(a) shows the predicted lifetime for semi-metallic UO₂ for various degrees of non-equilibrium between the electron and phonon temperatures. (Note that fast-ion stoppage creates a state of substantial non-equilibrium, as discussed in the Section 4.) Regardless of the non-equilibrium state, the strong EPC lowers the electron lifetime into the fs range at high temperatures.

Using this lifetime, we can calculate the electron thermal conductivity. The integral given in Eq. (3) is carried out in BoltzTrap [40] using the electron eigenstates from DFT-HSE and the lifetime given by the inverse of Eq. (9). The results are presented in Fig. 9(b) for various non-equilibrium conditions and pressures. As shown and as expected, the conductivity depends strongly on the degree

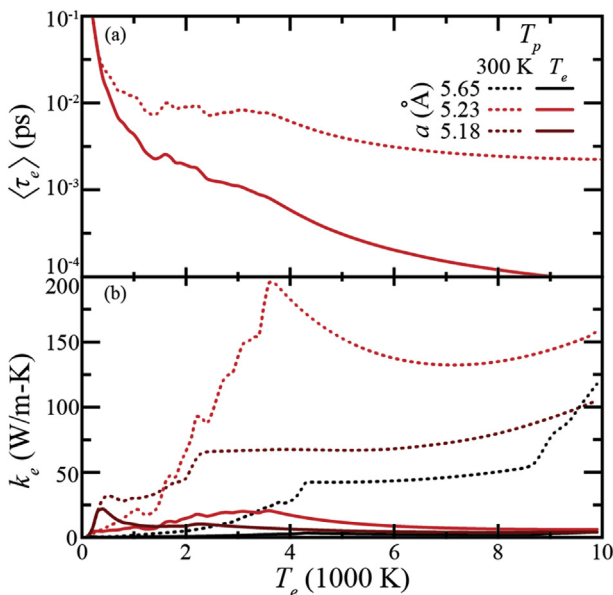


Fig. 9. Electron lifetime (a) and thermal conductivity (b) for variations in the electron temperature and electron-phonon non-equilibrium. Under equilibrium conditions, the conductivity is suppressed by the short electron lifetime.

of non-equilibrium and the transition of UO₂ from an insulator to a metal. For example, insulative UO₂ has a very low conductivity until the thermal energy approaches the bandgap and the conducting states are activated. At high temperatures, $T_e > 10,000$ K, insulating UO₂ approaches the thermal conductivity that highly pressurized, metallic/semi-metallic UO₂ has. However, even metallic and semi-metallic UO₂ has a relatively low thermal conductivity under equilibrium conditions, and substantial non-equilibrium is required to approach a thermal conductivity above 50 W/m-K (which, as we will discuss, is required for good agreement between the experiments and TTM + MD simulations). As extreme non-equilibrium is predicted within the TTM + MD simulations, we conclude that this order of thermal conductivity is achievable in pressurized, semi-metallic UO₂.

With the electronic contribution to the heat capacity and thermal conductivity evaluated, we require one final parameter for our TTM + MD simulations: The electron-phonon energy coupling parameter, G_{e-p} . Here we use the Eliashberg spectral function ($\alpha^2 F$) [45–48] to calculate G_{e-p} . This method is only applicable to the metallic UO₂, as it assumes that coupling is dominated by the electrons at the Fermi level. This theory and its assumptions were developed with superconductivity related phenomena in mind. Thus, it is most accurate at very low temperatures. However, it still enables a rough estimate of G_{e-p} . Given the other assumptions built into our treatment of the EPC, we must limit ourselves to this goal when evaluating both k_e and G_{e-p} .

In order to calculate G_{e-p} , we move through the dimensionless coupling,

$$\lambda_{\alpha}(\kappa_p) = \frac{1}{\omega_{\alpha,\kappa_p} D_e(E_F)} \sum_{i,j} \left| M_{e-p}^{ij,\alpha}(\kappa_e, \kappa_p) \right|^2 \delta(E_{e,\kappa_e,i} - E_F) \delta(E_{e,\kappa_e+\kappa_p,i} - E_F), \quad (10)$$

into the spectral function,

$$\alpha^2 F(\omega) = \frac{1}{2} \sum_{\alpha,\kappa_p} \omega_{\alpha,\kappa_p} \lambda_{\alpha}(\kappa_p) \delta(\omega_{\alpha,\kappa_p} - \omega), \quad (11)$$

and finally calculate the energy coupling [49],

$$G_{e-p} = \pi \hbar k_B D_e(E_F) \int_0^{\infty} \alpha^2 F(\omega) \omega d\omega. \quad (12)$$

Here we evaluate these integrals quantities using Lorentzian, rather than Dirac, δ functions. This greatly aids convergence and is generally necessary with the rough κ_e -meshes used in DFT simulations. Finally, we assume that the EPC matrix elements are independent of the phonon wavevector and that $|M_{e-p}^{ij,\alpha}(\kappa_e, \kappa_p)|^2 \approx |M_{e-p}^{ii,\alpha}(\kappa_e, \Gamma) M_{e-p}^{jj,\alpha}(\kappa_e + \kappa_p, \Gamma)|$. Under this assumption, the acoustic modes do not contribute to the spectral function or the energy coupling, G_{e-p} . While short-wavelength acoustic modes can contribute substantially to the electron-phonon coupling, the high frequency optical modes tend to dominate, as the integrand in Eq. (12) weights the spectral function by the phonon frequency. (Physically, this is because high frequency phonon modes exchange more energy with the electron system per interaction than the low-frequency modes do.) Thus, our assumption should enable an order-of-magnitude evaluation of G_{e-p} . As we show in Section 3, this is sufficient within the TTM + MD simulations.

The resulting spectral functions are shown in Fig. 10(a) for

variations in the pressure and smearing. The spectral function shows an interesting trend: The insulating and semi-conducting spectral functions have nearly identical shapes, with the three low-frequency optical phonon branches contributing equally, whereas the three high-frequency branches dominate the semi-metallic and metallic UO_2 spectral functions. The lower optical branches involve uranium motion while the upper branches do not. Thus, we hypothesize that the distance between the uranium atoms has less effect on the electron properties once the uranium atoms are sufficiently close, i.e., once UO_2 becomes semi-metallic or metallic. By integrating these spectral functions according to Eq. (12), we evaluate G_{e-p} . The results are presented in Fig. 10(b). As shown, the pressure has a large effect on the EPC. In particular, note that the δ functions in Eq. (11) ensure that the EPC vanishes when UO_2 is an insulator or semiconductor. The smeared, Lorentzian δ functions alleviate this, allowing for a reduced coupling between electronic states which are not on the Fermi-surface. Thus, the G_{e-p} can range between 0 and 10^{21} , depending on the smearing value in the insulating and semi-conducting UO_2 . Substantial smearing of the electron population does occur within our TTM + MD simulations, with electron temperatures in excess of 20,000 K. Indeed, a smearing of 0.26 eV (or approximately 3000 K) is not only physical, but conservative. Conversely, the Eliashberg spectral function approach is derived with a superconductivity (0 K metals) in mind. Thus, applying it to a 20,000 K insulator provides only approximate results, at best. However, we can see that the smearing of the Fermi surface has negligible effect on the EPC in the semi-metallic and metallic UO_2 , as one would hope. Regardless, we see that UO_2 can exhibit a substantial G_{e-p} : It always does under high pressures, and should at high temperatures and under low pressures. In the following section, we describe our TTM + MD model before exploring the implications of the *ab initio* parameterization described above.

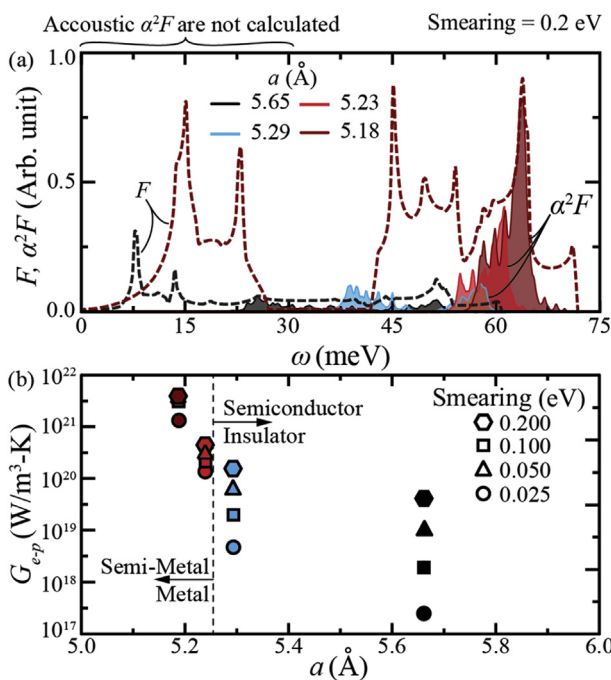


Fig. 10. (a) Phonon spectral function and density of states, F . The spectral functions are normalized by their total integral, while the phonon density of states is scaled such that the spectral function curves reside within it. (b) The electron-phonon coupling for the optical phonon modes in UO_2 . In the semi-metal and metal regime, the δ -function smearing negligible affects the EPC. In the semi-conducting and insulating regime, it has a very large effect, with a strictly enforced δ function (no smearing) leading to $G_{e-p} = 0$.

3. TTM + MD calculations

The two-temperature model (TTM) was firstly employed by Kaganov et al. [50], and Anisimov et al. [51] for the simulation of the hot electron excitation induced by femtosecond laser pulse. The model successfully explained the subsequent interaction between the cold lattice (phononic system) and the hot electron population, i.e., their equilibration and thermalization. Wang et al. [52] and Toulemonde et al. [53] noted that the electronic excitation induced by a laser pulse is analogous to that induced by swift heavy ions penetrating a metal and used the TTM simulate the subsequent electron-phonon equilibration and cooling processes. However, the TTM cannot simulate the formation of defects or an ion track formation. A recent approach remedies this shortcoming by combining TTM with classical MD to get more accurate description of the atomic dynamics, the production of defects, and the formation of an amorphized ion track [13].

In the TTM + MD model, energy exchange between the two subsystems (electronic, e , and phononic, p) is specified by the electron heat diffusion equation [22],

$$C_e(T_e) \frac{\partial T_e}{\partial t} = \nabla(k_e \nabla T_e) - G_{e-p}(T_e - T_p) + G_e T'_p, \quad (13)$$

where C_e , k_e and T are the heat capacity, number density, thermal conductivity and temperature, respectively. T'_p is the local temperature of atoms whose velocity is greater than the electronic stopping critical velocity. G_{e-p} is the electron-phonon coupling constant, and G_e is the electron stopping constant. Given an updated distribution of the phonon temperature (T_p), the spatial and temporal distributions of non-equilibrium electron temperature (T_e) are solved numerically using a finite difference method. Where the typical TTM model uses a heat diffusion equation for the phonon temperature, the TTM + MD model replaces this with the Langevin dynamics, as we discuss next.

Within the Langevin dynamics, the movement of atom i is governed by Refs. [13,22].

$$\mathbf{F}_i = -\frac{\partial U}{\partial \mathbf{r}_i} - \gamma \mathbf{v}_i + \mathbf{F}'_{lang}(t), \quad (14)$$

where \mathbf{F}_i is total force acting on atom i , U is the interatomic potential, γ is the friction-coefficient, and \mathbf{F}'_{lang} is the stochastic Langevin force term. Within the TTM + MD model, the friction and stochastic forces are determined by the electron-phonon coupling. In particular, the friction-coefficient γ considers the friction-like coupling between the atomic and electronic systems due to electronic stoppage (γ_e) or electron-phonon scattering (γ_{e-p}). These coefficients are related to the coupling coefficients G_{e-p} and G_e through the following equations

$$G_{e-p} = \frac{n_p c_p}{m} \gamma_{e-p}, \quad (15)$$

$$G_e = \frac{n'_p c_p}{m} \gamma_e, \quad (16)$$

where n_p is the concentration of ions and n'_p is the concentration of ions with a velocity greater than the electronic stopping critical velocity (v_0), m is the average atomic mass, and c_p is heat capacity of the lattice. Through these relationships, atoms moving faster than v_0 are damped by the electronic stopping and electron-phonon coupling ($\gamma = \gamma_{e-p} + \gamma_e$ and $G = G_e + G_{e-p}$), and atoms moving slower than v_0 are damped only by the electron-phonon coupling ($\gamma = \gamma_{e-p}$ and $G = G_{e-p}$). The Langevin force term (\mathbf{F}'_{lang}) exerts an

additional stochastic force on atom i in equilibrium state due to the electron-phonon coupling [13] via the fluctuation-dissipation theorem, as presented in eqs. (17) and (18).

$$\mathbf{F}'_{lang}(t) = 0, \quad (17)$$

$$\mathbf{F}'_{lang}(t) \cdot \mathbf{F}'_{lang}(t') = 2k_B T_e \gamma_{e-p} \delta(t' - t). \quad (18)$$

Under this framework, we require the *ab initio* properties collected in Section 2 (k_e , C_e , and G_{e-p}) as well as the electronic stopping friction coefficient (γ_e). In the following section, we calculate this term.

3.1. Electronic stoppage

Based on the Lindhard and Scharff model [5,54], the electronic energy loss (solid line in Fig. 11) in the low-energy regime is proportional to the square root of the kinetic energy of a particle (E) (Fig. 11).

$$\frac{dE}{dx} = \Lambda E^{1/2}, \quad (19)$$

where Λ is the constant of proportionality. Substituting the classical kinetic energy, we have

$$m \frac{dv}{dt} = \Lambda \left(\frac{m}{2}\right)^{1/2} v, \quad (20)$$

and with analogy to the friction term in the Langevin equation of motion in Eq. (14), we have

$$\gamma_e = \Lambda \left(\frac{m}{2}\right)^{1/2}. \quad (21)$$

Here, we determine this parameter by fitting the energy loss (dE/dx) of O^{16} and U^{238} to electrons in UO_2 , as predicted by the SRIM code. Fig. 11 shows the results of our SRIM simulations, where we can see the typical, proportionality for the electronic stopping given in Eq. (20). From these simulations, we calculate a γ_e of 162 g/mol-

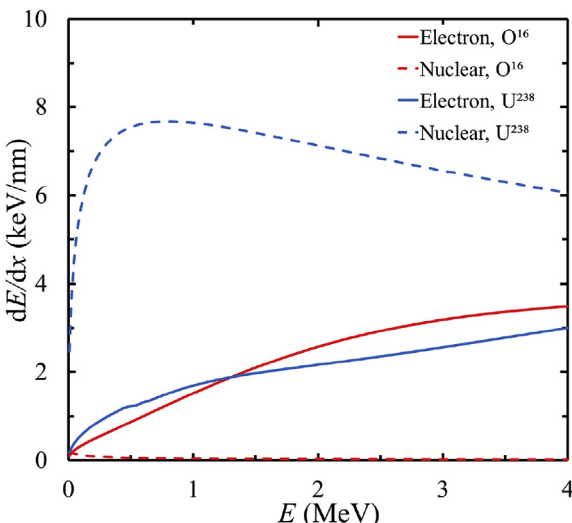


Fig. 11. Energy loss of O^{16} (red) and U^{238} (blue) calculated from the SRIM [6]. Both electronic (solid lines) and nuclear stopping (broken lines) powers are obtained. While oxygen and uranium contribute substantially to the electronic stoppage, uranium contributes dominantly to the nuclear stoppage. (For interpretation of the references to colour in this figure legend, the reader is referred to the Web version of this article.)

ps for U^{238} and 89 g/mol-ps for O^{16} , and we use the average of 114 g/mol-ps in our TTM + MD simulations. Additionally, we require the critical velocity. Here we use the velocity required to reach a kinetic energy doubling the cohesive energy per atom in UO_2 (13.52 eV), i.e., $v_0 = 7.62 \text{ nm/ps}$. With these two electronic stopping properties, we have the necessary parameters for the TTM + MD simulations. Now let us describe our simulation methodology.

3.2. System configuration and initial heat spike

We perform the TTM + MD simulations in a box with dimensions of $32.8 \times 32.8 \times 10.9 \text{ nm}^3$, corresponding to a $60 \times 60 \times 20$ supercell with 864,000 ions, and we discretize this simulation box into a $31 \times 31 \times 7$ mesh for the finite difference integration of the electron energy equation. We use the CRG interatomic potential [55] based on embedded-atom method (EAM) [56] for short-range forces with the long-range charge summation method PPPM for the long-range forces [57]. The CRG potential has been used to successfully reproduced the solid-state material properties (lattice parameters, lattice energy, and elastic constants) [55] and applied to the thermal transport [58–60] and defect dynamics [61,62]. Moreover, for the thermal spike region, material properties at extremely high temperatures (up to 5000 K) have also been successfully predicted using the CRG potential [63]. The LAMMPS simulation package [64] is used to integrate the Langevin dynamics [64] for TTM and the coupled electron energy equation [Eq. (13)] [22,65].

To initialize our system, we equilibrate a NPT ensemble of UO_2 atoms at 300 K for 1 ns with a 1 fs time step. Next, the initial electronic temperature is prescribed in order to mimic the electronic system in the wake of a swift heavy ion. Here we assume that initial heat spike morphology is cylindrically symmetric in the z -direction [39] and is given by a Gaussian distribution. This Gaussian distribution is determined using a modified form of the analytical thermal spike model (ATSM) [66–69]. That is,

$$\Delta T_e = \frac{S_e}{\rho_e c_{e,0} \pi \mu_e^2} \exp\left(-\frac{r^2}{\mu_e^2}\right), \quad (22)$$

where S_e is the initial energy deposited as a heat spike in the electronic subsystem, ρ_e and $c_{e,0}$ are the electronic density and saturated electronic specific heat, and μ_e is the penetration depth, which depends on the thermal diffusivity of the ionized electrons. Here we assume that it is 1.2 nm. Following initialization, the TTM + MD simulations are carried out in a confined simulation box for 50 ps with a 0.1 fs time step during the initial, irradiation regime and 150 ps with a 1 fs timestep for the subsequent recombination regime. During these (NVE) simulations, we use an outer cylindrical Langevin thermostat to avoid the asymmetry caused by a rectangular boundary. With our methodology established, let us discuss the parameterization of UO_2 in our TTM + MD model.

3.3. Parameterization and validation of TTM + MD

First, we note that our TTM + MD simulations assume that the thermal conductivity and electron-phonon coupling are constant and that the heat capacity depends only on the temperature. In reality, they depends on the pressure, electron and phonon temperatures, and the atomic and electronic configurations. For example, the material properties will be very different along the ion track during (i) the initial non-equilibrium period, (ii) the subsequent energy dissipation and damage-accumulation phase, (iii) the damage-recovery and nano-restructuring stage, and (iv) the return to equilibrium. (These phases will be discussed further in the Section 4.) Furthermore, the material properties along the ion track

differ substantially from those in the surrounding, undamaged UO_2 lattice. While our *ab initio* calculations incorporate the pressure and temperature dependence of the material properties, we cannot capture the importance of the atomic or electronic configurations. Indeed, accurate quantum-mechanical simulation of a melted or partially-melted, damaged UO_2 core surrounded by crystal UO_2 is precluded by the large number of atoms required to define this system. Still, our pressurized UO_2 calculations provide the first *ab initio* window into the material properties which determine the extent of the damage created by a swift heavy ion penetrating UO_2 .

As the TTM + MD framework was designed to capture and evaluate the accumulation of damage along the ion track, we focus on *ab initio* simulations of compressed, high-temperature UO_2 , i.e., the material properties of the ion track during phases (i) and (ii). Our *ab initio* simulations provide a range of properties for compressed UO_2 , which we summarize in Table 2. Additionally, this table shows the properties that have been used in previous TTM + MD simulations and the parameter set used here to get accurate predictions of the radiation damage. Before selecting the most appropriate parameters to use in our TTM + MD simulations, let us first show that the TTM + MD model can accurately predict the radiation damage and then discuss how our *ab initio* parameters affect the degree of damage caused by an energetic ion, as quantified by the track radius, R_t . Here, R_t is qualitatively determined by examining the extent of the amorphous state after equilibrium conditions return. The amorphous state is quantified by using the common neighbor analysis (CNA) [70] for the uranium ion sublattice and Wigner-Seitz analysis. In the CNA, the FCC and disordered regions of uranium ions are separated (after the oxygen ions are removed) in order to highlight the damaged region of the simulation box. After removing the pristine FCC sublattice, the R_t of the disordered region is qualitatively measured by fitting a cylinder within the track, as shown in Fig. 12(a). The maximal deviations of the track from this cylinder, δR_t , are also quantified. The Wigner-Seitz analysis provides similar results and validation of the CNA method by calculating the occupancy of defects within the simulation. While it does indicate a slightly smaller track radius, as shown in Fig. 12(b), this is expected, as the CNA examines the local structure environment based on the ionic pairs rather than the individual ions. In the following discussion, we use the Wigner-Seitz method to calculate the track radius.

Before proceeding, however, we must note that the TTM + MD solution becomes unstable as G_{e-p}/k_e becomes too large. In our simulations, this condition is approximately $G_{e-p}/k_e > 10^{17} \text{ m}^{-2}$, with a weak dependence on the lattice constant and thus $C_e(T_e)$. Thus, we had to limit the G_{e-p} to less than 10^{19} for the non-equilibrium parameter sets (where the conductivity is high) and

approximately 10^{17} or less for the equilibrium parameter sets. Thus, we present results for variations in G_{e-p} in order to explore the dependence of R_t on G_{e-p} and indicate whether our R_t predictions are an underestimation of the exact *ab initio* parameterizations given in Table 2.

As shown in green circles and triangles of Fig. 13(a), the stronger electron-phonon coupling is, the larger the track radii grows. This is expected. Consider the case where the electron phonon coupling is negligible, $G_{e-p}/k_{e-p} \rightarrow 0 \text{ m}^{-2}$. Under this condition, nearly all of the energy initially deposited in the electron subsystem along the ion path would spread out before it could substantially heat the fuel lattice, and no melting would occur. As the electron phonon coupling grows, however, the non-equilibrium between the electronic and phononic subsystems vanishes more and more quickly, less energy is conducted away from the ion track by the electron subsystem before the subsystems equilibrate, and the lattice thus reaches increasingly high temperatures. Indeed, as $G_{e-p} \rightarrow 10^{18} \text{ W/m}^2$, the non-equilibrium vanishes within a few hundred fs, at which point the quasi-equilibrium system reaches temperatures in excess of 10,000 K. Because the non-equilibrium vanishes so quickly, even as $G_{e-p} \rightarrow 10^{18}$, we expect that the strength of the electron-phonon coupling is most important between $10^{17} < G_{e-p} < 10^{19} \text{ W/m}^2$. In particular, we expect that for smaller values of G_{e-p} , no melting occurs, and that for larger values of G_{e-p} , the electron and phonon subsystems equilibrate so quickly that the lattice reaches similarly high temperatures. Unfortunately, the instability of our $G_{e-p} > 10^{19}$ simulations precludes our testing of this hypothesis.

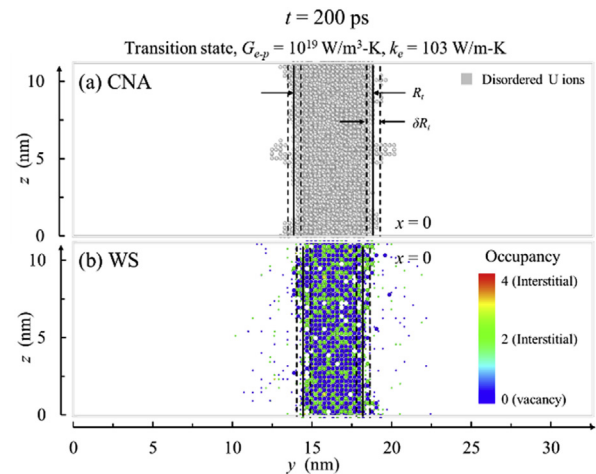


Fig. 12. Cross section of the (a) CNA and (b) WS analyses of the simulated ion track. The track radius is qualitatively determined by placing a cylinder within the track.

Table 2

Summary of the TTM + MD parameterization from *ab initio* simulations. Three rows are presented for the ground state, transition state, and Metallic state UO_2 simulations. These rows correspond to low-temperature ($T_e = T_p = 300 \text{ K}$), high temperature ($T_e = T_p = 10,000 \text{ K}$), and non-equilibrium conditions ($T_e = 10,000 \text{ K}$) and ($T_p = 300 \text{ K}$).

Parameter	$C_0 (\text{MJ/m}^3 \cdot \text{K})$	$C_1 (\text{MJ/m}^3 \cdot \text{K}^2)$	$C_2 (\text{MJ/m}^3 \cdot \text{K}^3)$	$C_3 (\text{MJ/m}^3 \cdot \text{K}^4)$	$C_4 (\text{MJ/m}^3 \cdot \text{K}^5)$	$T_o (\text{K})$	$C_p (\text{MJ/m}^3 \cdot \text{K})$	$M (\text{kg/kmol})$	$k_e (\text{W/m-K})$	$G_{e-p} (\text{W/m}^3 \cdot \text{K})$	$\gamma_e (\text{kg/kmol-ps})$	$v_0 (\text{nm/ps})$	$\mu_e (\text{nm})$
Literature	1.0 [71]	—	—	—	—	—	—	—	20 [10]	$10^{18} - 10^{19}$	—	—	—
Ground state ($a = 5.65 \text{ \AA}$)	0.79	2.56×10^{-5}	-5.49×10^{-8}	8.42×10^{-12}	-1.52×10^{-15}	4500	2.58 [72]	90	0.4 [2,71]	10^{17} [2,10,71]	114	7.6	1.5
Transition state ($a = 5.23 \text{ \AA}$)	0.82	1.80×10^{-5}	-4.35×10^{-8}	9.22×10^{-12}	-1.11×10^{-15}	4500	2.58 [72]	90	4.1	10^{19}	114	7.6	1.5
Metal state ($a = 5.18 \text{ \AA}$)	0.64	7.98×10^{-5}	1.97×10^{-9}	-3.11×10^{-12}	2.26×10^{-16}	4500	2.58 [72]	90	116	10^{19}	114	7.6	1.5
									4.8	10^{18}			
									6.1	10^{20}			
									155	10^{20}			
									19.7	10^{21}	114	7.6	1.5
									4.2	10^{21}			
									103	10^{21}			

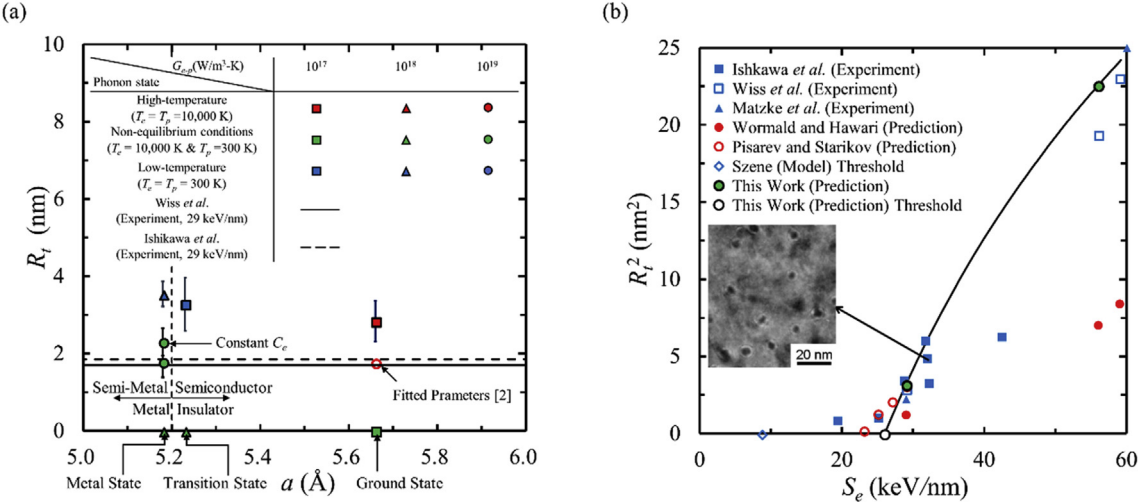


Fig. 13. (a) Track radius for an electronic stopping power of 29 keV/nm for variations in the electronic properties (as given in Table 2) and as compared to the experimentally determined track radii. Error bars represent the uncertainty of the track radius within a single simulation, ΔR_t . The thermal conductivity and electron-phonon coupling have a large effect on the agreement of TTM + MD with experiment. The electron-phonon coupling parametrization given on Table 2 causes instability in the TTM + MD solution, so variations are presented in order to establish the trends. (b) Square of the track radius as a function of stopping loss (S_e) in irradiated UO₂ for the most accurate parameterization set. (The inset TEM image is from Ishikawa et al. [75]).

Our results also show that the temperature dependence of the electronic heat capacity has a small but notable influence on the results. Note, for example, the discrepancy in the track radius for constant and T_e -dependent shown in Fig. 13(a) for the metallic, non-equilibrium parameter set. Thus, while using a constant or adjusted heat capacity relationships allows for stable TTM + MD solutions as G_{e-p}/k_e grows larger than 10^{17} m^{-2} , some notable error will result from such an approximation. With these trends established, let us move on to discuss the successes and failures of our *ab initio* parameter sets.

Our results tend to bracket the experimental track radii. In general, the equilibrium parameter sets overestimate the track radius while the non-equilibrium parameter sets underestimate the track radius. In these simulations, the non-equilibrium parameter sets underestimate the track radius because the electronic thermal transport is very fast. Indeed, the large electron thermal conductivity allows for a substantial proportion of the stopping energy to dissipate without causing damage. That is, the lattice at 10,000 K dissipates the stopping energy not through the propagation of phonons but by the ejection of ions from the lattice. Therefore, the more energy which is dissipated by the electron system, the less damage there is that accrues along the path of the ion and the smaller the track radius grows. In contrast, the equilibrium parameter sets overestimate the track radius because the electronic thermal transport is sluggish.

Of all of our parameterization sets, the metallic, non-equilibrium parameter set is the only one which leads to an accurate prediction of the track radii, as shown in Fig. 13(b) for variations in the electronic stopping power. Note that this result uses a reduced electron-phonon coupling in order to stabilize the TTM + MD simulation. Moreover, the non-equilibrium transport is not, in reality, so substantial or constant throughout the simulations. Thus, while the *ab initio* parameter set provides accurate predictions of the track radii and threshold stopping power, as shown in Fig. 13, the results should not be taken as proof that this *ab initio* parametrization accurately represents the conditions present during the dissipation of the electronic stopping power. Still, we can glean important information from this first effort towards an *ab initio* parametrized TTM + MD simulation. Moreover, we can suggest in which directions the TTM + MD and *ab initio*

study of electronic stopping in UO₂ should progress.

First, consider the TTM + MD simulations. A more realistic description of the electronic thermal transport would include the effects of the phonon occupation and electronic temperature, $k_e(T_p, T_e)$. Within a TTM + MD simulations using such a description, the track radius would lie somewhere between the non-equilibrium lower bound and equilibrium upper bound which bracket the experimental track radius. That is, it should lie closer to the experimental result. Therefore, we suggest that modeling $k_e(T_p, T_e)$ within TTM + MD is a worthwhile direction in which to advance the TTM methodology. Note that while the full, *ab initio* description of the electronic transport, $k_e(T_p, T_e, \Omega)$, remains well out-of-reach of *ab initio* simulation, accurate *ab initio* descriptions of $k_e(T_p, T_e)$ are not as far removed from current computational capabilities. (Here Ω describes the configuration and state of the UO₂ fuel.) Furthermore, rough calculations are currently possible, as in this study. Moreover, the TTM method presumes that the electron and phonon temperatures determine the electronic transport. Therefore, modeling $k_e(T_p, T_e)$ fits within the methodology, while modeling $k_e(T_p, T_e, \Omega)$ does not. Another worthwhile advance would be to include temperature dependence in the electron-phonon energy exchange, $G_{e-p}(T_e)$, as the electron temperature can lead to massive variations in this term.

Within the *ab initio* simulations, the most important direction is to increase the accuracy of the electron-phonon coupling calculations, as this greatly impacts both the transport and energy exchange parameters. At the moment, however, the accurate, *ab initio* calculation of the electron-phonon coupling in strongly correlated materials remains out of reach. This important topic remains an active, but numerically and computationally challenging one. In combination, however, we hypothesize that improved *ab initio* and TTM + MD simulations should enable a much more satisfying and accurate simulation of swift heavy ion damage in UO₂.

4. Damage processes, characteristics, and assessments

Here we consider simulations where the ion deposits 29 keV/nm in the electronic subsystem. This creates a large temperature spike in the electronic system which quickly and sharply increases the temperature in the phononic (atomic) subsystem through the

electron-phonon coupling. Indeed, Fig. 14(a and b) shows that the lattice reaches temperatures on the order of 10,000 K, well above its melting temperature (3183 K), within 100 fs. This high temperature induces a correspondingly large spike in pressure, with the central region experiencing pressures above 40 GPa, as shown in Fig. 14(c and d). The electron and phonon systems relax quickly as heat is conducted away from the ion track. Indeed, the thermal energy dissipates within 10 ps

While the pressure largely dissipates as well, a high pressure ring with a radius approximately equal to the track radius persists. This pressurized ring around the ion track arises due to the interaction between the melted ion track core (where a large number of

vacancies reduce the pressure), the interstitial defects clustered around this (which increase the pressure), and the relatively undamaged UO_2 lattice surrounding it (where the lattice mismatch induces some strain). These regions are shown in Fig. 14(e), where an occupancy of unity denotes the occupancy in undamaged UO_2 , such that an occupancy less (greater) than unity indicates the presence of vacancy (interstitial) defects. While some recombination of interstitial defects and vacancies occurs, as shown in Fig. 14(e and f), the diffusion of interstitial defects from outside to inside R_t (the core) is stopped the pressurized ring.

Indeed, the pair distribution function analysis for uranium shows that the electronic stopping creates an amorphous core, and

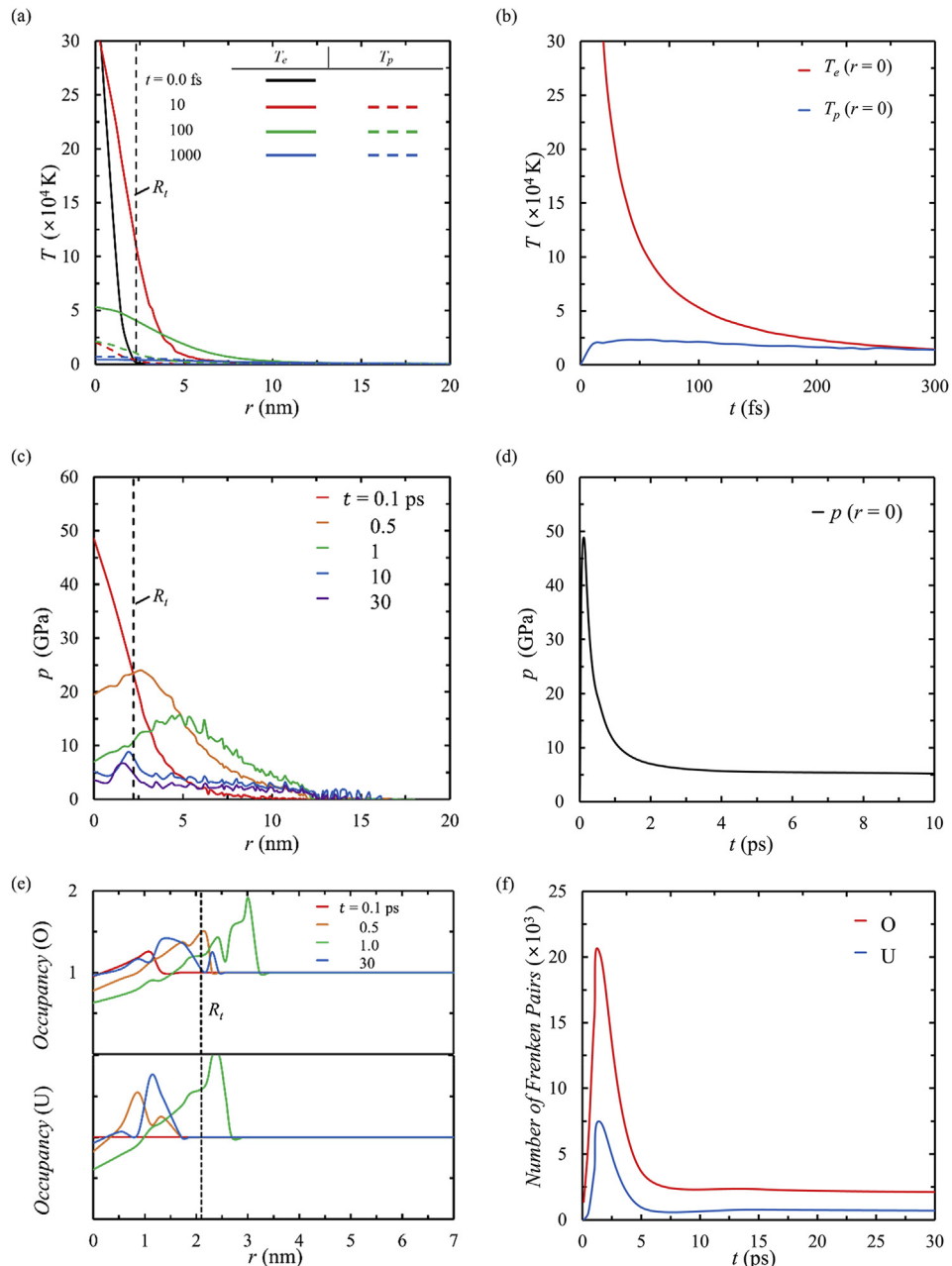


Fig. 14. Spatial and temporal variation of temperature, pressure and defects following a 29 keV/nm energy deposition (a) Temperatures of the electron and phonon subsystems at few selected times for variations in the distance from the ion track and (b) evolution of the temperature at the center of the track for the electron and phonon subsystems. (c) Pressure at a few selected times for variations in the distance from the ion track (averaged) and (d) the evolution of the pressure at the center of the track over time. (e) Radial distribution of the mean defect occupancy of ion sites at elapsed times of 0.1, 0.5, 1 and 15 ps for U and O ions. An occupancy of 1 represents undamaged UO_2 , while an occupancy less than (greater than) 1 represents the net presence of vacancy (interstitial) defects. (f) Evolution of Frenken pair formation for O and U ion.

it shows that the average U-U bond length decreases within the ion track, as shown in Fig. 15. While this decrease is negligible, the analysis does show that a substantial portion of the uranium atoms are separated by less space. We visualize the amorphous ion track using a Wigner-Seitz defect analysis [6], and it remains distinct, even as $t \rightarrow 200$ ps, as shown in Fig. 16. This analysis determines the defective points while removing the non-defect atoms in the cell. In Wigner – Seitz defect analysis, the defective points are determined by comparing the atomic positions within a pristine crystal to the current positions. Fig. 16, rendered by OVITO [77], shows the results. Within the first few ps, a large number of oxygen vacancies (blue) are created near the center of the ion track (now a molten, uranium-heavy core), while interstitial oxygen atoms (green – red) accumulate around this core. Following the pressure recovery and during the thermal recovery, many of these defects recombine. However, a distinct, amorphous core remains, as shown in Fig. 16(b), and as seen in experiments [73–76]. Next, let us characterize the total number of defects created during electronic stopping, as predicted within TTM + MD.

To do so, we first compare the vacancy production per distance within the SRIM and TTM + MD frameworks including the recombination regime (200 ps). Here the same incident ions and stopping loss values used in experiments [76] are used within SRIM, i.e., Xe¹²⁹ with an initial kinetic energy of 150 MeV and U²³⁸ with initial kinetic energy of 550 MeV. We simulate 5000 of them in order to calculate the average number of vacancies produced during electron stoppage. As shown in Table 3, the SRIM model underestimates the number of defects produced by these ions by two to three orders of magnitude when compared to our TTM + MD simulations. Note, however, that SRIM predicts many more defects by nuclear stopping than MD collision cascade simulation.

Let us expand our defect characterization and quantify the penetration depth of an incident ion using TTM + MD. To do this, we discretize the stopping energy loss relation calculated within SRIM [Fig. 17(a)] for a typical fission fragment produced by the fission of U²³⁵ following its capture of a thermal neutron. That is, we simulate the stoppage of fission fragment Xe¹³³ with 76 MeV of initial kinetic energy [78], rather than simulate the ions used in previous experiments (Xe¹²⁹ or U²³⁸ ion). Then, we use TTM + MD to calculate the number of defects by electronic stopping produced along the particle track. Next, we convert from the energy loss

domain to a physical, penetration depth domain. Finally, we compare the SRIM and TTM + MD predictions of defect production by electronic stopping per distance. Again, and as shown in Fig. 17(b), the TTM + MD model predicts that many more defects are created by electronic stopping than the SRIM simulations predict. Note that nuclear stopping is not considered in this work. Near the threshold stopping power, however, both models predict a similar number of defects are created along the ion track. Note that the defect creation from selected TTM parameters results in small variations in the log scale graph. Thus, we hypothesize that the SRIM model underestimates the number of defects created during the electronic stoppage, while overestimating the number of defects created during nuclear stoppage (due to non-existence of molecular dynamics in SRIM). Indeed, while the TTM + MD framework is explicitly built to capture the electron-phonon coupling, the large flow of energy from the electronic to phononic subsystems thereby, the massive pressure and temperature induced in the lattice, and the defects which result from these phenomena; SRIM is not.

From the defect estimation along the particle path, the spatial distribution of the atomic damage-per-atom (dpa) along the path of the incident particle is derived as an important description of the effective radiation damage at the engineering scale [19].

$$dpa(z) = \frac{\Phi(z)}{n_p} \frac{dn_v(z)}{dz}, \quad (23)$$

where Φ , n_p , dn_v/dz are the predetermined ion fluence distribution, atom number density and defect formation per distance, respectively. As we hypothesize that SRIM substantially underestimates the latter quantity, and that TTM + MD represents a substantial improvement over the SRIM model, we suggest that nuclear engineers adopt of TTM + MD as the standard when evaluating the dpa of nuclear-related materials.

5. Conclusions

We investigate the cascade of energy from the electron to atomic subsystems in UO₂, following the electronic stoppage of a swift heavy ion. In particular, we use a multiscale analysis to investigate the radiation damage which results from this energy cascade. We use *ab initio* (DFT-HSE) simulations to calculate the pressure and temperature dependent material properties of UO₂ in order to explore its transition from a dielectric to metal and the effects this has on nonequilibrium energy transport. Then, we use a combined macroscale-atomistic model (TTM + MD) with a parameterization informed by the aforementioned *ab initio* simulations in order to explore the mechanisms of radiation damage and validate our *ab initio* approximations.

In our *ab initio* simulations using the DFT-HSE framework, we support the previous calculations showing that UO₂ becomes metallic under high pressures. Furthermore, we calculate the electronic heat capacity and thermal conductivity, and the electron-phonon energy coupling of UO₂ for variations in the pressure and electron and phonon temperatures. We predict that pressurized, semi-metallic UO₂ is a relatively sluggish conductor due to its strong electron-phonon coupling. However, the large non-equilibrium between the electronic and phononic subsystems induced in UO₂ by the electronic stopping of a swift heavy ion enables fast thermal transport. Under such conditions, our *ab initio* simulations give us a range of parameterizations for our subsequent TTM + MD runs which enables their successful prediction of the track radius and threshold stopping power. Indeed, the metallic state UO₂ under strong non-equilibrium and with $G_{e-p} = 10^{19}$ W/m³·K provides a parametrization that enables the TTM + MD model

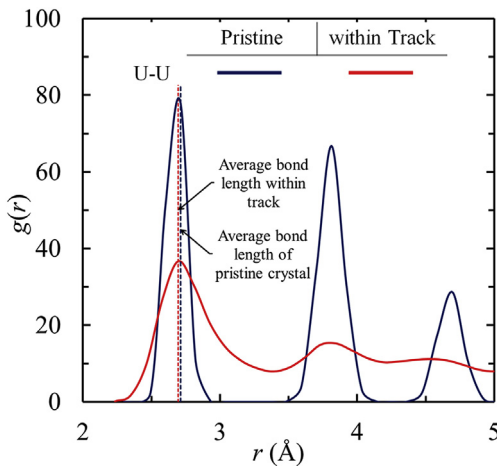


Fig. 15. Uranium distribution function in pristine UO₂ at 300 K and within the ion track after the simulation is complete. The disorder in the ion track leads to an increased smearing in the distribution function, while the oxygen vacancies allow for smaller interatomic (U-U) distances. However, the mode of the first nearest-neighbor U-U remains essentially the same.

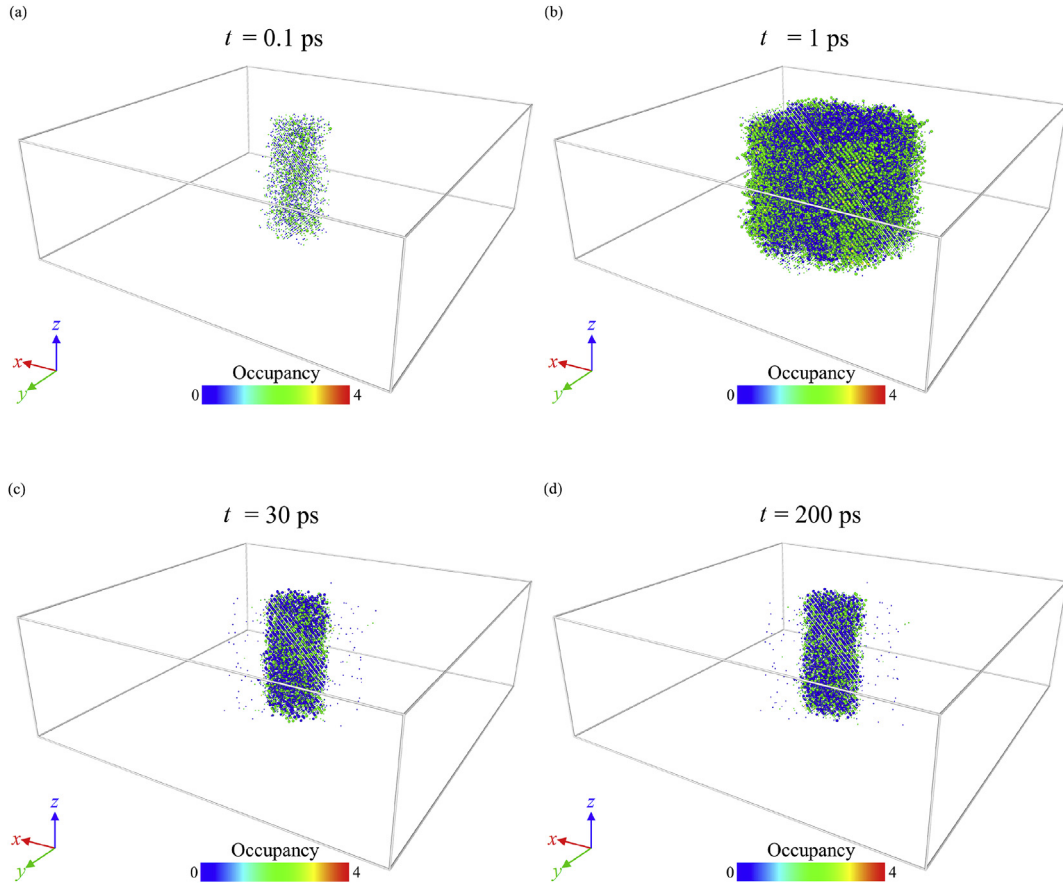


Fig. 16. Defect distribution within the simulation box after elapsed times of (a) 0.1 ps [phase (i)], (b) 1 ps [phase (ii)] (c) 30 ps [phase (iii)] and (d) 200 ps [phase (iv)] following a 29 keV/nm energy deposition.

to simulate damage and predict track radii in good agreement with the experimental results.

These TTM + MD runs, in addition to accurately reproducing the aforementioned experimental observations, provide a wealth of information on the damage processes which follow electronic stopping. In particular, we report the fs-scale evolution of the pressure, the subsystem temperatures, and the production and recombination of defects in the wake of a swift heavy ion penetrating UO₂. These analyses support the potential formation of a metallic UO₂ phase with good thermal transport. However, the track is amorphous and U-heavy, rather than crystalline, compressed UO₂. Additionally, the TTM + MD simulations use a set of constant-value, rather than pressure and temperature dependent, material properties (aside from the heat capacity, which does depend on the electron temperature). Thus, the multiscale analysis only gives a plausible explanation of the apparent, metallic behavior, and it only provides a rough outline of the energy cascade and damage which follows swift heavy ion penetration. With these

caveats, our analysis still provides useful results and suggestions for improvement of both the *ab initio* and TTM + MD investigations.

In particular, we suggest that a TTM + MD solver which successfully incorporates the effects on non-equilibrium on the electronic thermal transport, $k_e(T_e, T_p)$, should lead to more successful and meaningful *ab initio* parameterization. Furthermore, the *ab initio* parameterization itself should advance through the relaxation of a number of approximations. Crucial among these is the development of accurate electron-phonon coupling codes for strongly correlated systems implemented within the DFT or DFT + DMFT methodologies.

Furthermore, we evaluate the defect creation from electronic stoppage along the particle path by transforming the TTM + MD simulations from the damage-per-energy to a damage-per-length scale and show its applicability to the dpa evaluation over the μm -scale of the ion track using our nm-scale TTM + MD simulations. This analysis shows that much more damage occurs within the radiation track during electronic stopping than is predicted

Table 3

Comparison of defect formation per angstrom between TTM + MD simulation and SRIM codes with Kinchin-Pease quick and full cascade calculations for 29 (Xe¹²⁹ ion) and 56 keV/nm (U²³⁸ ion) of electronic energy loss.

Method	dn_v/dz (1/Å-ion)	
	29 keV/nm (Xe ¹²⁹)	56 keV/nm (U ²³⁸)
SRIM-2008, Kinchin-Pease quick calculation [18]	0.10 (150 MeV, Initial step)	0.16 (550 MeV, Initial step)
SRIM-2008, Full Cascade calculation [18]	0.15 (150 MeV, Initial step)	0.16 (550 MeV, Initial step)
TTM + MD	33	135

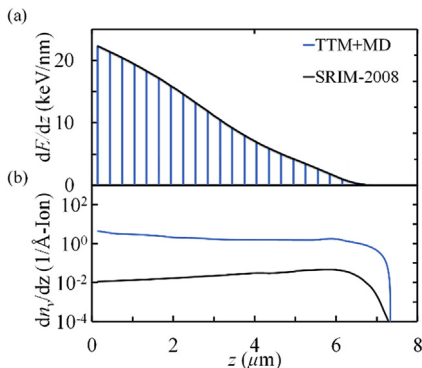


Fig. 17. (a) Electronic stopping loss of Xe^{133} ion having 76 MeV of initial energy along the penetration path in UO_2 (Black line) calculated by SRIM codes and the discretization of the stopping power for input of TTM + MD simulations (Blue bars). (b) Comparison of resultant defect formation per depth of penetration by SRIM (Black line) and TTM + MD (Blue line). (For interpretation of the references to colour in this figure legend, the reader is referred to the Web version of this article.)

within the more common SRIM model. We show that this increase in damage is due to the electron-phonon coupling, which is not captured within the SRIM model. Indeed, if combined with the existing collision cascade MD simulation for nuclear stoppage, we propose that the TTM + MD framework can be used for a more accurate approach to evaluating the overall dpa of the irradiated material by both the electronic and nuclear stoppage. This framework, based on multiscale approach, is applicable to other metallic alloys under fission, fusion or irradiation by incident ions.

Acknowledgement

This research was supported by National Nuclear R&D Program through the National Research Foundation of Korea funded by the Ministry of Science and ICT (NRF-2017M2B2A9072831) and Basic Science Research Program through the National Research Foundation of Korea(NRF) funded by the Ministry of Education (2018R1A6A3A01011475). We used computational resources of the National Energy Research Scientific Computing Center, a DOE Office of Science User Facility supported by the Office of Science of the U.S. Department of Energy under Contract No. DE-AC02-05CH11231 and the resources of Korea Institute of Science and Technology Information under Contract No. KSC-2018-G3-0002. We are thankful to Dr. Duck Young Kim (Center for High Pressure Science & Technology Advanced Research, Shanghai, China) for suggestion of pressure metallization of U-O compounds.

References

- [1] J.J. Duderstadt, L.J. Hamilton, *Nuclear Reactor Analysis*, Wiley, New York, 1976.
- [2] V. V Pisarev, S. V Starikov, Atomistic simulation of ion track formation in UO_2 , *J. Phys. Condens. Matter* 26 (2014) 475401, <https://doi.org/10.1088/0953-8984/26/47/475401>.
- [3] B. Ziaja, R.A. London, J. Hajdu, Unified model of secondary electron cascades in diamond, *J. Appl. Phys.* 97 (2005), <https://doi.org/10.1063/1.1853494>.
- [4] S. Bouffard, B. Gervais, C. Leroy, Basic phenomena induced by swift heavy ions in polymers, *Nucl. Instrum. Meth. Phys. Res. B* 105 (1995) 1–4, [https://doi.org/10.1016/0168-583X\(95\)00525-0](https://doi.org/10.1016/0168-583X(95)00525-0).
- [5] J. Lindhard, M. Scharff, H.E. Schiøtt, *Range Concepts and Heavy Ion Ranges*, Munksgaard Copenhagen, 1963.
- [6] K. Nordlund, M. Ghaly, R.S. Averback, M. Caturla, T. Diaz de la Rubia, J. Tarus, Defect production in collision cascades in elemental semiconductors and fcc metals, *Phys. Rev. B* 57 (1998) 7556–7570, <https://doi.org/10.1103/PhysRevB.57.7556>.
- [7] T.D. de la Rubia, R.S. Averback, H. Hsieh, R. Benedek, Molecular dynamics simulation of displacement cascades in Cu and Ni: thermal spike behavior, *J. Mater. Res.* 4 (1989) 579–586.
- [8] G.P. Srivastava, *The Physics of Phonons*, CRC press, 1990.
- [9] C. Melnick, M. Kaviany, M.H. Kim, Roles of core-shell and d-ray kinetics in layered BN a-voltaic efficiency, *J. Appl. Phys.* 113 (2013) 1–8, <https://doi.org/10.1063/1.4790506>.
- [10] J.L. Wormald, A.I. Hawari, Examination of the impact of electron–phonon coupling on fission enhanced diffusion in uranium dioxide using classical molecular dynamics, *J. Mater. Res.* 30 (2015) 1485–1494, <https://doi.org/10.1557/jmr.2014.405>.
- [11] B.P. Uberuaga, R. Smith, A.R. Cleave, F. Montalenti, G. Henkelman, R.W. Grimes, A.F. Voter, K.E. Sickafus, Structure and mobility of defects formed from collision cascades in MgO , *Phys. Rev. Lett.* 92 (2004) 115505.
- [12] X.-M. Bai, A.F. Voter, R.G. Hoagland, M. Nastasi, B.P. Uberuaga, Efficient annealing of radiation damage near grain boundaries via interstitial emission, *Science* 327 (2010) 1631–1634, <https://doi.org/10.1126/science.1183723>.
- [13] A. Rutherford, D. Duffy, The effect of electron-ion interactions on radiation damage simulations, *J. Phys. Condens. Matter* 19 (2007) 1–9, <https://doi.org/10.1088/0953-8984/19/49/496201>.
- [14] G.J. Ackland, Comprehensive nuclear materials, in: *Compr. Nucl. Mater.*, Elsevier, Amsterdam, AE, 2012, pp. 267–291, <https://doi.org/10.1016/B978-0-08-056033-5.00026-4>.
- [15] K.E. Sickafus, E.A. Kotomin, B.P. Uberuaga, *Radiation Effects in Solids*, Springer Science & Business Media, 2007.
- [16] K.E. Sickafus, L. Minervini, R.W. Grimes, J.A. Valdez, M. Ishimaru, F. Li, K.J. McClellan, T. Hartmann, Radiation tolerance of complex oxides, *Science* (80) 289 (2000) 748–751.
- [17] K.E. Sickafus, R.W. Grimes, J.A. Valdez, A. Cleave, M. Tang, M. Ishimaru, S.M. Corish, C.R. Stanek, B.P. Uberuaga, Radiation-induced amorphization resistance and radiation tolerance in structurally related oxides, *Nat. Mater.* 6 (2007) 217–223.
- [18] J.F. Ziegler, M.D. Ziegler, J.P. Biersack, SRIM: the stopping and range of ions in matter, *Nucl. Instrum. Methods Phys. Res. Sect. B Beam Interact. Mater. Atoms* 268 (2010) 1818–1823, <https://doi.org/10.1016/j.nimb.2010.02.091>.
- [19] R.E. Stoller, M.B. Toloczko, G.S. Was, A.G. Certain, S. Dwarkanath, F.A. Garner, On the use of SRIM for computing radiation damage exposure, *Nucl. Instrum. Methods Phys. Res. Sect. B Beam Interact. Mater. Atoms* 310 (2013) 75–80, <https://doi.org/10.1016/j.nimb.2013.05.008>.
- [20] R.S. Averback, T.D. de la Rubia, Displacement damage in irradiated metals and semiconductors, *Solid State Phys.* 51 (1997) 281–402.
- [21] P. Partyka, Y. Zhong, K. Nordlund, R.S. Averback, I.M. Robinson, P. Ehrhart, Grazing incidence diffuse x-ray scattering investigation of the properties of irradiation-induced point defects in silicon, *Phys. Rev. B* 64 (2001) 235207.
- [22] D.M. Duffy, a M. Rutherford, Including the effects of electronic stopping and electron–ion interactions in radiation damage simulations, *J. Phys. Condens. Matter* 19 (2007) 16207, <https://doi.org/10.1088/0953-8984/19/1/016207>.
- [23] L. Huang, Y. Wang, P. Werner, Orbital-selective Mott Transition and Evolution of the Zhang–Rice State in Cubic Phase UO_2 under Pressure, 2015, pp. 3–7, arXiv Preprint. arXiv:1506.06548.
- [24] B.C. Frazer, G. Shirane, D.E. Cox, C.E. Olsen, Neutron-Diffraction study of antiferromagnetism in UO_2 , *Phys. Rev.* 140 (1965) A1448.
- [25] B.T.M. Willis, R.I. Taylor, Neutron diffraction study of antiferromagnetism in UO_2 , *Phys. Lett.* 17 (1965) 188–190.
- [26] I.D. Prodan, G.E. Scuseria, R.L. Martin, Assessment of metageneralized gradient approximation and screened Coulomb hybrid density functionals on bulk actinide oxides, *Phys. Rev. B* 73 (2006) 45104.
- [27] L.E. Roy, T. Durakiewicz, R.L. Martin, J.E. Peralta, G.E. Scuseria, C.G. Olson, J.J. Joyce, E. Guziewicz, Dispersion in the Mott insulator UO_2 : a comparison of photoemission spectroscopy and screened hybrid density functional theory, *J. Comput. Chem.* 29 (2008) 2288–2294.
- [28] S.L. Dudarev, G.A. Botton, S.Y. Savrasov, C.J. Humphreys, A.P. Sutton, Electron-energy-loss spectra and the structural stability of nickel oxide: an LSDA+ U study, *Phys. Rev. B* 57 (1998) 1505.
- [29] J. Heyd, G.E. Scuseria, M. Ernzerhof, Erratum: hybrid functionals based on a screened Coulomb potential, *J. Chem. Phys.* 124 (2006) 219906.
- [30] J. Heyd, G.E. Scuseria, M. Ernzerhof, Hybrid functionals based on a screened Coulomb potential, *J. Chem. Phys.* 118 (2003) 8207–8215.
- [31] B.T. Wang, P. Zhang, R. Lizárraga, I.D. Marco, O. Eriksson, Phonon spectrum, thermodynamic properties, and pressure–temperature phase diagram of uranium dioxide, *Phys. Rev. B* 88 (2013) 104107.
- [32] X.-D. Wen, R.L. Marin, T.M. Henderson, G.E. Scuseria, *Chem. Rev.* 113 (2013) 1063.
- [33] M. Idiri, T. Le Bihan, S. Heatherman, J. Rebizant, Behavior of actinide dioxides under pressure: UO_2 and ThO_2 , *Phys. Rev. B* 70 (2004), 014113.
- [34] M.S.S. Brooks, P.J. Kelly, On the cohesive energy and charge density of uranium dioxide, *Solid State Commun.* 45 (1983) 689.
- [35] Y. Baer, J. Schoenes, Electronic structure and coulomb correlation energy in UO_2 single crystal, *Solid State Commun.* 33 (1980) 885.
- [36] P. Giannozzi, O. Andreussi, T. Brumme, O. Bunau, M.B. Nardelli, M. Calandra, R. Car, C. Cavazzoni, D. Ceresoli, M. Cococcioni, Advanced capabilities for materials modelling with Quantum ESPRESSO, *J. Phys. Condens. Matter* 29 (2017) 465901.
- [37] P. Giannozzi, S. Baroni, N. Bonini, M. Calandra, R. Car, C. Cavazzoni, D. Ceresoli, G.L. Chiarotti, M. Cococcioni, I. Dabo, A.D. Corso, S. de Gironcoli, S. Fabris, G. Fratesi, R. Gebauer, U. Gerstmann, C. Gougaud, A. Kokalj, M. Lazzeri, L. Martin-Samos, N. Marzari, F. Mauri, R. Mazzarello, S. Paolini, A. Pasquarello, L. Paulatto, C. Sbraccia, S. Scandolo, G. Sclauzero, A.P. Seitsonen, A. Smogunov, P. Umari, R.M. Wentzcovitch, QUANTUM ESPRESSO: a modular and open-

- source software project for quantum simulations of materials, *J. Phys. Condens. Matter* 21 (2009) 395502. <http://stacks.iop.org/0953-8984/21/i=39/a=395502>.
- [38] N. Troullier, J.L. Martins, Efficient pseudopotentials for plane-wave calculations, *Phys. Rev. B* 43 (1991) 1993.
- [39] M. Kaviany, in: Heat Transfer Physics, second ed., Cambridge University Press, New York, NY, 2014 <https://doi.org/10.1017/CBO9780511754586>.
- [40] G.K.H. Madsen, D.J. Singh, BoltzTrap. A code for calculating band-structure dependent quantities, *Comput. Phys. Commun.* 175 (2006) 67–71.
- [41] S. Baroni, S. De Gironcoli, A. Dal Corso, P. Giannozzi, Phonons and related crystal properties from density-functional perturbation theory, *Rev. Mod. Phys.* 73 (2001) 515.
- [42] Y. Yun, D. Legut, P.M. Oppeneer, Phonon spectrum, thermal expansion and heat capacity of UO₂ from first-principles, *J. Nucl. Mater.* 426 (2012) 109–114.
- [43] G. Dolling, R.A. Cowley, A.D.B. Woods, The crystal dynamics of uranium dioxide, *Can. J. Phys.* 43 (1965) 1397–1413, <https://doi.org/10.1139/p65-135>.
- [44] M. Lundstrom, Fundamentals of Carrier Transport, Cambridge University Press, 2009.
- [45] T. Livneh, Coupling of multi-LO phonons to crystal-field excitations in UO₂ studied by Raman spectroscopy, *J. Phys. Condens. Matter* 20 (2008) 85202.
- [46] P.B. Allen, Neutron spectroscopy of superconductors, *Phys. Rev. B* 6 (1972) 2577–2579, <https://doi.org/10.1103/PhysRevB.6.2577>.
- [47] P.B. Allen, Electron-phonon effects in the infrared properties of metals, *Phys. Rev. B* 3 (1971) 305–320, <https://doi.org/10.1103/PhysRevB.3.305>.
- [48] F. Giustino, Electron-phonon interactions from first principles, *Rev. Mod. Phys.* 89 (2017) 1–63, <https://doi.org/10.1103/RevModPhys.89.015003>.
- [49] Z. Lin, L.V. Zhigilei, V. Celli, Electron-phonon coupling and electron heat capacity of metals under conditions of strong electron-phonon nonequilibrium, *Phys. Rev. B Condens. Matter* 77 (2008) 1–17, <https://doi.org/10.1103/PhysRevB.77.075133>.
- [50] M.I. Kaganov, Relaxation between electrons and the crystalline lattice, *Sov. Phys. JETP* 4 (1957) 173–178.
- [51] S.I. Anisimov, Emission of electrons from the surface of metals induced by ultrashort laser pulses, *Sov. Phys. JETP* 39 (1974) 375.
- [52] Z.G. Wang, C. Dufour, E. Paumier, M. Toulemonde, The Se sensitivity of metals under swift-heavy-ion irradiation: a transient thermal process, *J. Phys. Condens. Matter* 6 (1994) 6733, <https://doi.org/10.1088/0953-8984/6/34/006>.
- [53] M. Toulemonde, E. Paumier, C. Dufour, Thermal spike model in the electronic stopping power regime, *Radiat. Eff. Defect Solid* 126 (1993) 201–206, <https://doi.org/10.1080/10420159308219709>.
- [54] J. Lindhard, M. Scharff, Energy dissipation by ions in the keV region, *Phys. Rev.* 124 (1961) 128.
- [55] M.W.D. Cooper, M.J.D. Rushton, R.W. Grimes, A many-body potential approach to modelling the thermomechanical properties of actinide oxides, *J. Phys. Condens. Matter* 26 (2014) 105401, <https://doi.org/10.1088/0953-8984/26/10/105401>.
- [56] M.S. Daw, M.I. Baskes, Embedded-atom method: derivation and application to impurities, surfaces, and other defects in metals, *Phys. Rev. B* 29 (1984) 6443–6453, <https://doi.org/10.1103/PhysRevB.29.6443>.
- [57] E.L. Pollock, J. Glosli, Comments on P3M, FMM, and the Ewald method for large periodic Coulombic systems, *Comput. Phys. Commun.* 95 (1996) 93–110, [https://doi.org/10.1016/0010-4655\(96\)00043-4](https://doi.org/10.1016/0010-4655(96)00043-4).
- [58] W.K. Kim, J.H. Shim, M. Kaviany, UO₂ bicrystal phonon grain-boundary resistance by molecular dynamics and predictive models, *Int. J. Heat Mass Tran.* 100 (2016) 243–249, <https://doi.org/10.1016/j.ijheatmasstransfer.2016.04.071>.
- [59] M.J. Qin, M.W.D. Cooper, E.Y. Kuo, M.J.D. Rushton, R.W. Grimes, G.R. Lumpkin, S.C. Middleburgh, Thermal conductivity and energetic recoils in UO₂ using a many-body potential model, *J. Phys. Condens. Matter* 26 (2014) 495401.
- [60] M.W.D. Cooper, S.C. Middleburgh, R.W. Grimes, Modelling the thermal conductivity of (U_x Th_{1-x})O₂ and (U_x Pu_{1-x})O₂, *J. Nucl. Mater.* 466 (2015) 29–35.
- [61] A. Chroneos, R.V. Vovk, Modeling self-diffusion in UO₂ and ThO₂ by connecting point defect parameters with bulk properties, *Solid State Ionics* 274 (2015) 1–3.
- [62] M.W.D. Cooper, S.T. Murphy, P.C.M. Fossati, M.J.D. Rushton, R.W. Grimes, Thermophysical and anion diffusion properties of (U_x Th_{1-x})O₂, in: *Proc. R. Soc. London A Math. Phys. Eng. Sci. The Royal Society*, 2014, p. 20140427.
- [63] J.H.S. and M.K. Woong Kee Kim, Thermophysical Properties of Liquid UO₂, ZrO₂ and Corium by ECMD, (n.d.).
- [64] S. Plimpton, Fast parallel algorithms for short-range molecular dynamics, *J. Comput. Phys.* 117 (1995) 1–19, <https://doi.org/10.1006/jcph.1995.1039>.
- [65] D.M. Duffy, N. Itoh, a M. Rutherford, a M. Stoneham, Making tracks in metals, *J. Phys. Condens. Matter* 20 (2008) 82201, <https://doi.org/10.1088/0953-8984/20/8/082201>.
- [66] G. Szenes, General features of latent track formation in magnetic insulators irradiated with swift heavy ions, *Phys. Rev. B* 51 (1995) 8026–8029, <https://doi.org/10.1103/PhysRevB.51.8026>.
- [67] G. Szenes, Thermal spike model of amorphous track formation in insulators irradiated by swift heavy ions, *Nucl. Instrum. Methods Phys. Res. Sect. B Beam Interact. Mater. Atoms* 116 (1996) 141–144, [https://doi.org/10.1016/0168-583X\(96\)00025-0](https://doi.org/10.1016/0168-583X(96)00025-0).
- [68] G. Szenes, Comparison of two thermal spike models for ion-solid interaction, *Nucl. Instrum. Methods Phys. Res. Sect. B Beam Interact. Mater. Atoms* 269 (2011) 174–179, <https://doi.org/10.1016/j.nimb.2010.11.009>.
- [69] G. Szenes, Ion-induced amorphization in ceramic materials, *J. Nucl. Mater.* 336 (2005) 81–89, <https://doi.org/10.1016/j.jnucmat.2004.09.004>.
- [70] J.D. Honeycutt, H.C. Andersen, Molecular dynamics study of melting and freezing of small Lennard-Jones clusters, *J. Phys. Chem.* 91 (1987) 4950–4963.
- [71] M. Huang, D. Schwen, R.S. Averback, Molecular dynamic simulation of fission fragment induced thermal spikes in UO₂: sputtering and bubble re-solution, *J. Nucl. Mater.* 399 (2010) 175–180, <https://doi.org/10.1016/j.jnucmat.2010.01.015>.
- [72] P.J. W, C.J. Kim, Y-E, Thermophysical Properties Database of Materials for Light Water Reactors and Heavy Water Reactors, International Atomic Energy Agency, 2006.
- [73] H. Matzke, P.G. Lucuta, T. Wiss, Swift heavy ion and fission damage effects in UO₂, *Nucl. Instrum. Methods Phys. Res. Sect. B Beam Interact. Mater. Atoms* 166 (2000) 920–926, [https://doi.org/10.1016/S0168-583X\(99\)00801-0](https://doi.org/10.1016/S0168-583X(99)00801-0).
- [74] N. Itoh, D.M. Duffy, S. Khakshouri, A.M. Stoneham, Making tracks: electronic excitation roles in forming swift heavy ion tracks, *J. Phys. Condens. Matter* 21 (2009) 474205, <https://doi.org/10.1088/0953-8984/21/47/474205>.
- [75] N. Ishikawa, T. Sonoda, T. Sawabe, H. Sugai, M. Satake, Electronic stopping power dependence of ion-track size in UO₂ irradiated with heavy ions in the energy range of ~1 MeV/u, *Nucl. Instrum. Methods Phys. Res. Sect. B Beam Interact. Mater. Atoms* 314 (2013) 180–184, <https://doi.org/10.1016/j.nimb.2013.05.038>.
- [76] T. Wiss, H. Matzke, C. Trautmann, M. Toulemonde, S. Klaumünzer, Radiation damage in UO₂ by swift heavy ions, *Nucl. Instrum. Methods Phys. Res. Sect. B Beam Interact. Mater. Atoms* 122 (1997) 583–588, [https://doi.org/10.1016/S0168-583X\(96\)00754-9](https://doi.org/10.1016/S0168-583X(96)00754-9).
- [77] A. Stukowski, Visualization and analysis of atomistic simulation data with OVITO—the Open Visualization Tool, *Model. Simulat. Mater. Sci. Eng.* 18 (2009) 15012, <https://doi.org/10.1088/0965-0393/18/1/015012>.
- [78] J. Randrup, R. Vogt, Calculation of fission observables through event-by-event simulation, *Phys. Rev. C: Nucl. Phys.* 80 (2009) 1–11, <https://doi.org/10.1103/PhysRevC.80.024601>.